Theory of x-ray photon correlation spectroscopy for multiscale flows

Hao Yin ⬤ *

Department of Mechanical Engineering, University of Rochester, Rochester, New York 14627, USA
and Center for Matter at Atomic Pressures, University of Rochester, Rochester, New York 14627, USA

Charles Heaton ⬤

Department of Physics, University of Oxford, Parks Rd, Oxford OX1 3PU, United Kingdom

Eric G. Blackman ⬤

Department of Physics and Astronomy, University of Rochester, New York 14627, USA;
Center for Matter at Atomic Pressures, University of Rochester, Rochester, New York 14627, USA;
and Laboratory for Laser Energetics, University of Rochester, Rochester, New York 14623, USA

Arianna E. Gleason ⬤

SLAC National Accelerator Laboratory, 2575 Sand Hill Road, Menlo Park, California 94025, USA

Joshua J. Turner

SLAC National Accelerator Laboratory, 2575 Sand Hill Road, Menlo Park, California 94025, USA
and Stanford Institute for Materials and Energy Sciences, Stanford University, Stanford, California 94305, USA

Gilbert W. Collins

Department of Mechanical Engineering, University of Rochester, Rochester, New York 14627, USA;
Department of Physics and Astronomy, University of Rochester, New York 14627, USA;
Center for Matter at Atomic Pressures, University of Rochester, Rochester, New York 14627, USA;
and Laboratory for Laser Energetics, University of Rochester, Rochester, New York 14623, USA

Gianluca Gregori ⬤

Department of Physics, University of Oxford, Parks Rd, Oxford OX1 3PU, United Kingdom

Jessica K. Shang ⬤ †

Department of Mechanical Engineering, University of Rochester, Rochester, New York 14627, USA;
Center for Matter at Atomic Pressures, University of Rochester, Rochester, New York 14627, USA;
and Laboratory for Laser Energetics, University of Rochester, Rochester, New York 14623, USA

Hussein Aluie ⬤ ‡

Department of Mechanical Engineering, University of Rochester, Rochester, New York 14627, USA;
Department of Mathematics, University of Rochester, Rochester, New York 14627, USA;
Center for Matter at Atomic Pressures, University of Rochester, Rochester, New York 14627, USA;
and Laboratory for Laser Energetics, University of Rochester, Rochester, New York 14623, USA

Complex multiscale flows associated with instabilities and turbulence are commonly induced under high-energy density (HED) conditions, but accurate measurement of their transport properties has been challenging. X-ray photon correlation spectroscopy (XPCS) with coherent x-ray sources can, in principle, probe material dynamics to infer transport properties using time autocorrelation of density fluctuations. Here we develop a theoretical framework for utilizing XPCS to study material diffusivity in multiscale flows. We extend single-scale shear flow theories to broadband flows using a multiscale analysis that captures shear and diffusion dynamics. Our theory is validated with simulated XPCS for Brownian particles advected in multiscale flows.

---

*Contact author: hyin8@me.rochester.edu
†Contact author: j.k.shang@rochester.edu
‡Contact author: hussein@rochester.edu

We demonstrate the versatility of the method over several orders of magnitude in timescale using sequential-pulse XPCS, single-pulse x-ray speckle visibility spectroscopy (XSVS), and double-pulse XSVS.

I. INTRODUCTION

X-ray photon correlation spectroscopy (XPCS) is an experimental technique that leverages coherent x-rays to investigate material dynamics at the microscopic scale [1,2]. XPCS is the x-ray equivalent of dynamic light scattering (DLS) [1,3,4]. While both DLS and XPCS aim to characterize the time evolution of density fluctuations within samples, XPCS can probe dynamics at nanometer length scales, which are smaller than those accessible by DLS due to the shorter wavelength of x-rays. State-of-the-art x-ray free-electron lasers (XFELs) deliver ultrashort x-ray pulses in the femtosecond range with high peak brightness [5,6] and can produce pulses with short separations [7], which are advantages over synchrotrons for applications requiring high temporal resolution. Pulses generated by XFELs also have high-degree coherence, which refers to the consistent phase difference of waves over time and space, leading to wave interference that provides information about the structure of a material. When coherent x-rays are scattered off a sample, an area detector captures the interference of scattered waves. The intensity distribution on the area detector is a so-called speckle pattern for its granular shape, where each speckle pattern reveals spatial density distribution in the sample. Thus, by collecting a batch of speckle patterns, the temporal dynamics of the material can be explored using intensity autocorrelation in time [8–10]. The Siegert relation [11,12] is then often used to link the intensity autocorrelation with the underlying density autocorrelation, providing a quantitative characterization of material dynamics.

Accurately approximating transport properties such as viscosity and diffusivity in warm dense matter has been a challenge, where different theoretical models often yield estimates differing by several orders of magnitude [13–15]. XPCS is a general and model-independent technique that provides the capability to probe material dynamics [16–18], including the direct measurement of transport properties such as diffusivity. Using sequential x-ray pulses, conventional XPCS can capture material dynamics across timescales from microseconds to hours [19,20].

In high-energy-density (HED) conditions, probing ultrafast dynamics is required since the characteristic timescales, such as the transit time of shock compression (the time for net flow to pass through the probe volume), are typically on the order of nanoseconds or less [21,22]. With different x-ray pulse structures [7,23] that allow access to ultrafast dynamics, x-ray speckle visibility spectroscopy (XSVS) can be used to extract dynamic information where the signal to noise ratio is not typically adequate [24–26]. XSVS analyzes the contrast, i.e., variance in intensity, of a partially coherent speckle pattern generated by a continuous beam (with the timescale given by the exposure time) or by integrated scattering from one or more short pulses (with the timescale of the pulse width, or pulse separation time, respectively). With short pulses, the timescale of diagnostic ranges from 100 femtoseconds to nanoseconds [20]. XSVS is particularly useful for studying ultrafast dynamics in high-energy-density systems or in the physics of phase transitions, while also in cases that require a low dose of radiation, such as in biological materials [27–29]. For single-pulse mode and two-bunch mode (or the split-and-delay method), XSVS is typically used to analyze the contrast of the generated single-pulse, or additive-pulse, speckle patterns. Here, we use the terms single-pulse XSVS and double-pulse XSVS to distinguish these two common cases, the latter sometimes referred to as x-ray photon fluctuation spectroscopy [30].

In HED conditions, shear flows are frequently induced in shocked material from defects or inhomogeneous structures [22,31–35]. Shear flows can influence diffusivity and viscosity measurements using XPCS [36–39]. In shear flows, particle motion can be attributed to two factors, shear and free diffusion, which are only easily distinguishable if their respective timescales differ significantly at a certain wave vector [40], so that one dominates the intensity autocorrelation in XPCS analysis. Fast shocks can make shear flows significant compared to free diffusion, but also result in comparable timescales between shear and diffusion in small-angle scattering (see an example of comparison between shear and diffusion timescale in Sec. III C). Although wide-angle scattering can be conducted by increasing the wavevector $|\mathbf{q}|$ (proportional to the sine of the scattering angle), to highlight the diffusion dynamics, the increase in the path length difference of the scattered photons leads to variations in phase differences. This challenges the analyses by reducing contrast from the limited coherence length of the x-ray beam, and the experimental setup [41].

If the shear flow is unidirectional, the effect of shear on XPCS analysis is extractable by inspecting the wave vector, $\mathbf{q}$, perpendicular to the shear direction [42]. However, this is not possible when shear is not unidirectional, as is likely in most HED applications. For example, in inertial confinement fusion (ICF) experiments, multiscale shear flows commonly arise from instabilities and turbulence [31,43,44]. Like in ICF, there are many experiments using laser shock compression to achieve HED conditions. We expect the outcome of this work to be beneficial for the XPCS analysis in such cases [45], as multiscale flows are likely to occur when a high-speed shock passes through the target due to porosity or defects. This work focuses on the XPCS theory in the presence of isotropic multiscale shear, meaning many small-scale shear flows are oriented randomly over the volume of interest. For anisotropic shear that may emerge [46–48], further investigation is required to modify the analytical equations [49]. Since the wavevector $\mathbf{q}$ is related to the flow direction, the anisotropy limits the XPCS analysis to a constrained angle in $\mathbf{q}$ space and requires high photon flux to compensate for the loss in statistics. This emphasizes the advantage of working with small-angle scattering at low $|\mathbf{q}|$ to obtain more photons recorded by the detector.
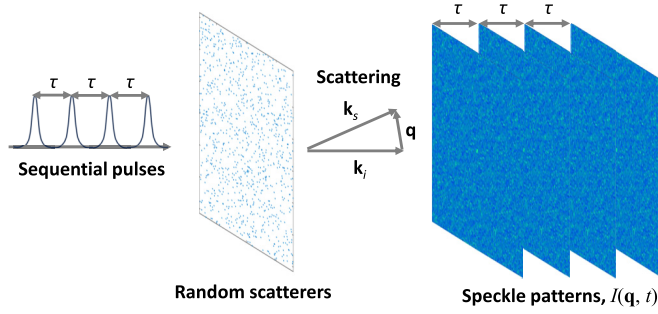
FIG. 1. Schematic of sequential-pulse XPCS. Coherent x-rays are scattered at a wavevector $\mathbf{q} = \mathbf{k}_s - \mathbf{k}_i$, for which the magnitude is proportional to the sine of the scattering angle. The intensity distribution on each speckle pattern, $I(\mathbf{q}, t)$, is recorded by the detector with a time separation τ corresponding to the time separation between the sequential pulses.

Previous works [36,37,39,50] have demonstrated that a uniform shear with constant shear rate $\dot{\gamma}$ can be characterized as a single-scale shear, where velocity fluctuation occurs in a single scale of the domain size. It leads to extra decay on intensity autocorrelation beyond free diffusion, corresponding to enhanced density fluctuations from the Siegert relation. In this work, we extend the theoretical framework to account for isotropic multiscale shear. We develop a methodology to identify a timescale associated with multiscale shear by Fourier decomposing multiscale flows. Thus, we distinguish the contribution of multiscale shear and free diffusion in sequential-pulse XPCS, single-pulse XSVS, and double-pulse XSVS at $\mathbf{q}$ even where their timescales are comparable. We use simulated XPCS that analyzes speckle patterns generated by scattering simulations to replicate the full process of an XPCS experiment. Through simulated XPCS, we measure the diffusion coefficient and the characteristic shear velocity on Brownian particles in isotropic multiscale flows to validate the multiscale theory.

In Sec. II, we describe the method of conducting simulated XPCS. We introduce the theory of sequential-pulse XPCS for free diffusion and uniform shear to validate the simulated XPCS results. In Sec. III, we perform simulated XPCS on passive particles with free diffusion advected by a multiscale shear flow. We demonstrate the generalization of single-scale theory to multiscales with the stretched exponential approximation, and propose a timescale for estimating the diffusion coefficient. In Sec. IV, we extend the multiscale theory to single-pulse exposure or double-pulse mode analyzed by XSVS to estimate the diffusion coefficient and characteristic shear velocity. We summarize the results in Sec. V.

II. SEQUENTIAL-PULSE XPCS

When a coherent x-ray beam is scattered by a sample, as sketched in Fig. 1, the scattering intensity is captured over a range of scattering wavevectors $\mathbf{q}$ simultaneously, where $\mathbf{q}$ is the difference between the diffracted wavevector $\mathbf{k}_s$ and the incoming wavevector, $\mathbf{k}_i$, i.e., $\mathbf{q} = \mathbf{k}_s - \mathbf{k}_i$. For complete elastic scattering, the photon energy remains unchanged after scattering, which leads to identical magnitudes between the incoming and scattered wavevector, $|\mathbf{k}_i| = |\mathbf{k}_s| = 2\pi/\lambda$,

where λ is the photon wavelength. We show the schematics of sequential-pulse XPCS in Fig. 1, where the wavevector $\mathbf{q}$ is directly proportional to the sine of the scattering angle.

The second-order correlation function, g_2, is the normalized intensity autocorrelation in time,

$$g_2(\mathbf{q}, \tau) = \frac{\langle I(\mathbf{q}, t) I(\mathbf{q}, t + \tau) \rangle_t}{\langle I(\mathbf{q}, t) \rangle_t^2}, \quad (1)$$

where τ is the time delay or separation between the sequential x-ray pulses, $I(\mathbf{q}, t)$ is the scattering intensity and $\langle \ldots \rangle_t$ denotes the time average over times t. The second-order correlation function can also be expressed by the Siegert relation [11,12],

$$g_2(\mathbf{q}, \tau) = 1 + \beta_0(\mathbf{q}) |F(\mathbf{q}, \tau)|^2. \quad (2)$$

The optical contrast, $\beta_0(\mathbf{q})$, measures the degree of coherence varying from 0 (incoherent illumination) to 1 (coherent illumination) relying on the beam coherence and the experimental setup, which is defined by the normalized intensity variance,

$$\beta_0(\mathbf{q}) = \frac{\langle I(\mathbf{q}, t)^2 \rangle_t - \langle I(\mathbf{q}, t) \rangle_t^2}{\langle I(\mathbf{q}, t) \rangle_t^2}. \quad (3)$$

$F(\mathbf{q}, \tau)$ in Eq. (2) is the intermediate scattering function (ISF), which is a first-order correlation function representing the spatial Fourier transform of the spatial and temporal density autocorrelation [51],

$$F(\mathbf{q}, \tau) = \int_V \langle \rho(\mathbf{r}_0, t) \rho(\mathbf{r}_0 + \mathbf{r}, t + \tau) \rangle_{\mathbf{r}_0, t} e^{i\mathbf{q} \cdot \mathbf{r}} d^3\mathbf{r}. \quad (4)$$

The decorrelation of $|F(\mathbf{q}, \tau)|^2$ is directly related to the material dynamics. We will focus on the trend of $|F(\mathbf{q}, \tau)|^2$ to retrieve transport properties assuming that the optical contrast in our simulated XPCS is $\beta_0(\mathbf{q}) = 1$ under a fully coherent beam. This condition holds for perfectly monochromatic x-rays, for an appropriate detector distance, and if the sample volume is contained within the coherence volume [41,52].

A. Scattering simulation

In simulated XPCS, we simulate x-ray scattering to generate speckle patterns for XPCS analysis. We reference the direct computational approach by Mohanty *et al.* [53] for generating simulated speckle patterns. At each time step, the displacement of each scatterer is tracked to generate a speckle pattern. In the simulation with diffusive and shear motion, the probe particles act as passive tracers, which perform free diffusion and are passively advected by the flow field. To describe the particle density distribution, a density field is defined as the sum of ith particle density at position $\mathbf{r}$,

$$\rho(\mathbf{r}, t) = \sum_{i=1}^{N} \rho_i(\mathbf{r}, t), \quad (5)$$

where $\rho_i(\mathbf{r}, t) = \delta(\mathbf{r} - \mathbf{r}_i(t))$ is a Dirac delta function centered at ith particle, and N is the number of particles. In the remaining equations, the sum over particle indices is from 1 to N unless otherwise specified. The Fourier transform of the density field is given by

$$\hat{\rho}(\mathbf{q}, t) = \int_V \sum_i \rho_i(\mathbf{r}, t) e^{-i\mathbf{q} \cdot \mathbf{r}} d^3\mathbf{r} = \sum_i f_i(\mathbf{q}) e^{-i\mathbf{q} \cdot \mathbf{r}_i(t)}, \quad (6)$$

where $f_i(\mathbf{q})$ is the x-ray form factor representing the Fourier transform of the ith particle's electron density distribution, ρ_e, about its center of mass ($\mathbf{r} = \mathbf{r}_i$),

$$f_i(\mathbf{q}) = \int_V \rho_e(\mathbf{r}) e^{-i\mathbf{q}\cdot(\mathbf{r}-\mathbf{r}_i)} d^3\mathbf{r}. \qquad (7)$$

The scattering intensity can be expressed by the square of the Fourier transformed density [53],

$$\begin{aligned} I(\mathbf{q}, t) &= \hat{\rho}(\mathbf{q}, t)\hat{\rho}^*(\mathbf{q}, t) = |\hat{\rho}(\mathbf{q}, t)|^2 \\ &= \sum_i f_i(\mathbf{q}) e^{-i\mathbf{q}\cdot\mathbf{r}_i(t)} \sum_j f_j(\mathbf{q}) e^{i\mathbf{q}\cdot\mathbf{r}_j(t)}, \end{aligned} \qquad (8)$$

where * is the complex conjugate. The scattering intensity is proportional to the Fourier transform of the electron density autocorrelation in space, $\langle\rho(\mathbf{r}_0, t)\rho(\mathbf{r}_0 + \mathbf{r}, t)\rangle_{\mathbf{r}_0}$ (Wiener-Khinchin theorem [54]).

Alternatively, $I(\mathbf{q}, t)$ can be written in a combined term,

$$I(\mathbf{q}, t) = \sum_i \sum_j f_i(\mathbf{q}) f_j(\mathbf{q}) e^{-i\mathbf{q}\cdot[\mathbf{r}_i(t)-\mathbf{r}_j(t)]}. \qquad (9)$$

The $f(\mathbf{q})$ and scattering intensity increase with the atomic number, Z, as x-rays are scattered by the electron cloud of the atom. In some experiments, high-Z nanoparticles (e.g., gold nanoparticles) are used to raise the scattering intensity [55–57]. The $f(\mathbf{q})$ for the same type or material of particle is invariant for all particles at any fixed $\mathbf{q}$. Under such condition, the autocorrelation function is independent of particle type as $f(\mathbf{q})$ is eliminated through normalization in Eq. (1). For simulated XPCS, we use Eqs. (1), (3), and (9) to simulate the squared ISF,

$$|F(\mathbf{q}, \tau)|^2_{\text{sim}} = (g_2(\mathbf{q}, \tau) - 1)/\beta_0(\mathbf{q}). \qquad (10)$$

B. Analytical solutions of squared ISF

To validate our simulated XPCS results, we compare the simulated squared ISF to analytical solutions. The ISF in Eq. (4) can be expressed using the Fourier transformed density in Eq. (6),

$$F(\mathbf{q}, \tau) = \frac{1}{N} \left\langle \sum_i \sum_j e^{-i\mathbf{q}\cdot[\mathbf{r}_i(t)-\mathbf{r}_j(t+\tau)]} \right\rangle_t. \qquad (11)$$

The factor $1/N$ appears to yield a normalized function that describes the dynamics in the system, regardless of the total number of particles. Assume particles are noninteracting and statistically independent, then we eliminate all cases in the sum when $i \neq j$, and the ISF is given by [37,58],

$$F(\mathbf{q}, \tau) = \frac{1}{N} \left\langle \sum_j e^{-i\mathbf{q}\cdot[\mathbf{r}_j(t)-\mathbf{r}_j(t+\tau)]} \right\rangle_t. \qquad (12)$$

Furthermore, each particle displacement, $\mathbf{r}_j(t + \tau) - \mathbf{r}_j(t)$, is attributed to displacements due to net flow through the probe volume, particle diffusion, and shear flow. The ISF can be separated into a product of transit, diffusion and shear components,

$$|F(\mathbf{q}, \tau)|^2 = |F_T(\mathbf{q}, \tau)|^2 |F_D(\mathbf{q}, \tau)|^2 |F_S(\mathbf{q}, \tau)|^2. \qquad (13)$$

Separating the ISF into the product in Eq. (13) had been justified in past studies under the assumption that timescales of the three processes are well separated [58,59].

In high-speed shear flows and conditions with large diffusivity, such as in HED, it is possible to observe similar timescales for diffusion and shear. In our study, instead of assuming that these timescales are separated, the product in Eq. (13) is valid under the assumption that the three processes (transit, diffusion, and shear) causing particle displacements are uncorrelated [60], as we will now elaborate. An ISF can be written as $F(\mathbf{q}, \tau) = \langle e^{-i\mathbf{q}\cdot\Delta\mathbf{r}(\tau)} \rangle$ where the $\langle\ldots\rangle$ is an average over time t and over particles j as in Eq. (12). Ignoring transit by bulk advection for now, the total displacement due to diffusion, $\Delta\mathbf{r}_D(\tau)$, and shear, $\Delta\mathbf{r}_S(\tau)$, is a linear superposition, $\Delta\mathbf{r}_D(\tau) + \Delta\mathbf{r}_S(\tau)$, giving the ISF, $F(\mathbf{q}, \tau) = \langle e^{-i\mathbf{q}\cdot\Delta\mathbf{r}_D(\tau)} e^{-i\mathbf{q}\cdot\Delta\mathbf{r}_S(\tau)} \rangle$. Knowing that for two uncorrelated events A and B, the expected value of their product follows the relation $E[AB] = E[A]E[B]$. The ISF can be written as the product $F(\mathbf{q}, \tau) = \langle e^{-i\mathbf{q}\cdot\Delta\mathbf{r}_D(\tau)} \rangle \langle e^{-i\mathbf{q}\cdot\Delta\mathbf{r}_S(\tau)} \rangle$.

For each component in Eq. (13), the contribution to particle displacement can be represented as $\mathbf{v}_T \tau$ (transit), $[\mathbf{r}'_j(t + \tau) - \mathbf{r}'_j(t)]$ (diffusion) and $\delta\mathbf{v}_j\tau$ (shear), where $\mathbf{v}_T$ is the transit velocity and $\delta\mathbf{v}_j$ is the difference between the flow velocity of the particle j and the mean flow velocity. This gives the product in the following form,

$$|F(\mathbf{q}, \tau)|^2 = |e^{i\mathbf{q}\cdot\mathbf{v}_T\tau}|^2 \times \left| \frac{1}{N} \left\langle \sum_j e^{-i\mathbf{q}\cdot[\mathbf{r}'_j(t)-\mathbf{r}'_j(t+\tau)]} \right\rangle_t \right|^2$$

$$\times \left| \frac{1}{N} \sum_j e^{-i\mathbf{q}\cdot\delta\mathbf{v}_j\tau} \right|^2. \qquad (14)$$

Within this product, the shear flow is assumed to be quasisteady and the shear velocity is statistically invariant over the time delay τ. We will neglect the transit component in this work with periodic boundary conditions for particle displacement and flow velocity fields. We will denote the wave vector magnitude $|\mathbf{q}|$ with q in the rest of this work if there is no risk of ambiguity.

For particles undergoing free diffusion (i.e., particles' mean-squared displacement, $\frac{1}{N}\sum_i |\mathbf{r}_i(t) - \mathbf{r}_i(0)|^2$, is proportional to t), the analytical solution of squared ISF [1] is given by,

$$|F_D(q, \tau)|^2 = \exp(-2Dq^2\tau), \qquad (15)$$

where D is the particle diffusion coefficient. The diffusion timescale is $\tau_D = 1/Dq^2$.

In the case of uniform shear with unidirectional flow velocity, u_x, along the x axis, difference in $\delta\mathbf{v}$ from Eq. (14) at any two positions in the two-dimensional (2D) velocity field can be expressed as $\delta v_{12} = \delta v_1 - \delta v_2 = \dot{\gamma}(y_1 - y_2)$, where y is in the varying direction of velocity. Integrating the last term in Eq. (14) with respect to y over the field size, previous studies [50,58] have derived

$$|F_S^{\text{uniform}}(q, \tau)|^2 = \frac{\sin^2(v_0 q_\parallel \tau/2)}{(v_0 q_\parallel \tau/2)^2}, \qquad (16)$$

where $q_\parallel$ is oriented in the wave vector space parallel to the flow direction (x axis in our case, $q_\parallel = q_x$) and the char-

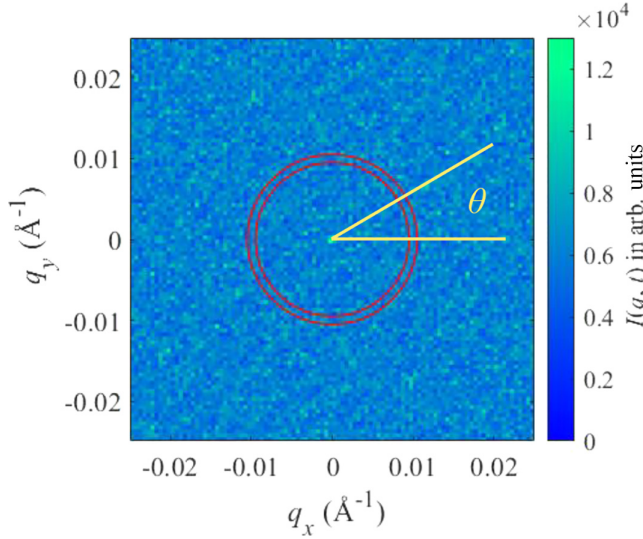FIG. 2. Visualization of a speckle pattern obtained from the simulated scattering with free diffusion ($D = 1 \times 10^{-3}\ cm^2/s$) and shear ($v_0 = 0.1$ μm/ns). The area encompassed in the red circles represents $q = 0.01 \pm 5 \times 10^{-4}$ Å^{-1} and angle θ is counterclockwise from the positive q_x axis in $q_x q_y$ plane.

acteristic shear velocity is $v_0 = \dot{\gamma}L = (du_x/dy)L$, with the field size L. Note that v_0 is characterized by shear flow and is distinct from the particle velocity difference $\delta\mathbf{v}_j$. The timescale for ISF decay due to shear is $\tau_S = 1/v_0 q_{\parallel}$ taking τ_S at $|F_S^{\text{uniform}}(q, \tau)|^2 = \sin^2(1/2)/(1/2)^2$.

C. Simulated XPCS with uniform shear

Mohanty *et al.* [53] have used molecular dynamics to simulate free diffusion without the shear component in simulated XPCS. Here, we simulate Brownian particles using a stochastic equation to validate simulated XPCS with a predefined diffusion coefficient. We verify simulated XPCS by comparing the square of simulated ISF to analytical solutions in three test cases: (i) free diffusion, (ii) uniform shear, and (iii) free diffusion combined with uniform shear through linear superposition of velocity. In all three cases, we initialize 10^4 point particles with uniform random distribution in a 2D periodic box of size 2π μm. We use the stochastic equation [61] to track the particle trajectory at each time step,

$$d\mathbf{x}(t) = \mathbf{u}(\mathbf{x}, t)dt + \sqrt{2D}\, d\mathbf{W}(t), \qquad (17)$$

where $\mathbf{x}(t)$ is the particle position, $\mathbf{u}(\mathbf{x}, t)$ is the flow velocity field, D is the particle diffusion coefficient, and $\mathbf{W}(t)$ denotes the Wiener process (Brownian motion) that follows a Gaussian random distribution with zero mean and unit variance. The flow field (deterministic part) and the Wiener process (stochastic part) are uncorrelated in Eq. (17).

We use the method described in Sec. II A to simulate the squared ISF in Eq. (10) at $q = 0.01 \pm 5 \times 10^{-4}$ Å^{-1} for q in between the red circles in Fig. 2. In the free diffusion case, we set the diffusion coefficient $D = 1 \times 10^{-3}$ cm^2/s in Eq. (17) and the displacement due to flow velocity term vanishes. In the uniform shear case, the velocity of the unidirectional flow varies linearly from 0–0.1 μm/ns (i.e., characteristic
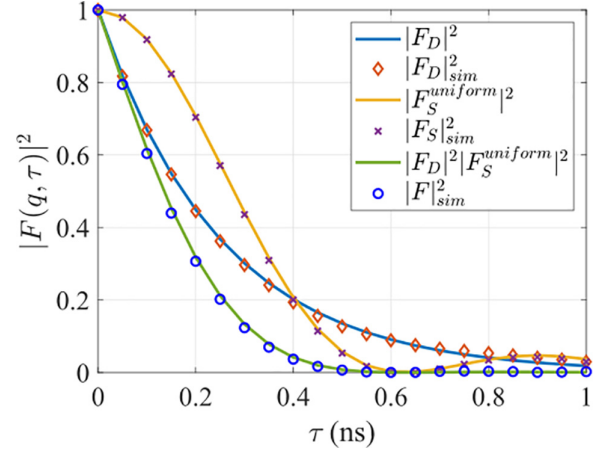

FIG. 3. Validation of the simulated squared ISF in diffusion, shear and combined cases ($|F_D|_{\text{sim}}^2$, $|F_S|_{\text{sim}}^2$ and $|F|_{\text{sim}}^2$ using Eq. (10)) by comparing to analytical equations ($|F_D|^2$, $|F_S^{\text{uniform}}|^2$, and $|F_D|^2|F_S^{\text{uniform}}|^2$) for free diffusion in uniform shear at $q_{\parallel} = 0.01 \pm 5 \times 10^{-4}$ Å^{-1}. $|F_D|^2$ is the diffusion component, $|F_D|^2 = e^{-2Dq^2\tau}$, and $|F_S^{\text{uniform}}|^2$ is the shear component, $|F_S^{\text{uniform}}|^2 = \sin{(v_0 q\tau/2)^2}/(v_0 q\tau/2)^2$, of the $|F(q, \tau)|^2$, where $D = 1 \times 10^{-3}$ cm^2/s and $v_0 = 0.1$ μm/ns.

shear velocity $v_0 = 0.1$ μm/ns), causing a deterministic solution without the Brownian motion term in Eq. (17). In the last case, both terms in Eq. (17) contribute to the particle displacement ($D = 1 \times 10^{-3}$ cm^2/s and $v_0 = 0.1$ μm/ns). In Fig. 3, we show that the simulated squared ISFs in all three cases follow the analytical solutions ($|F_D|^2 = e^{-2Dq^2\tau}$, $|F_S^{\text{uniform}}|^2 = \sin{(v_0 q\tau/2)^2}/(v_0 q\tau/2)^2$, and $|F_D|^2|F_S^{\text{uniform}}|^2 = e^{-2Dq^2\tau} \sin{(v_0 q\tau/2)^2}/(v_0 q\tau/2)^2$) with absolute errors within 5% for $\mathbf{q}$ along $q_{\parallel}$. The decomposition of $F(q, \tau)$ in Eqs. (13) and (14) is verified and the multiplication $|F_D|^2|F_S^{\text{uniform}}|^2$ leads to extra decay in ISF compared to the diffusion only and shear only cases. This implies the $|F(q, \tau)|^2$ decay is determined by both the diffusion and shear terms with timescales $\tau_D = 1\ ns$ and $\tau_S = 0.1\ ns$.

III. XPCS FOR MULTISCALE FLOWS

In practice, most flows are multiscale since energy tends to transfer across different scales [62]. In other words, even with a single-scale energy injection, single-scale flows can easily develop into multiscale flows due to perturbations. Turbulence and instabilities are two examples that represent multiscale flows developed through energy transfer across scales [47,63–66]. Multiscale flows are characterized by kinetic energy distribution over a broad range of length scales, implying that shear flows exist at various length scales, which cannot be directly described by XPCS for uniform shear. In this study, we apply Fourier analysis to decompose multiscale flows into single-scale flows. We generalize the XPCS theory of single-scale flows to multiscale flows using the properties of Fourier transform, kinetic energy conservation, and the orthogonality of Fourier modes [67].

Here, we conduct simulated XPCS using fully developed homogeneous turbulence from the Johns Hopkins Turbulence Database (JHTDB) [68] with a domain size of $L = 2\pi$ μm, as

well as a synthetically modified flow field that represents the case of instability to demonstrate the universality of the multiscale theory. The forced isotropic turbulence from JHTDB is simulated with the direct numerical simulation, which has the original size of 1024^3 nodes and 5028 timesteps. The statistical quality of the simulated XPCS is directly related to the number of speckle patterns. From photon statistics [11], the variance of g_2 is inversely proportional to the total number of correlated pairs, which implies more frames of intensity distribution to be averaged results in better statistics and less error in Eq. (1). Thus, we conduct the simulated XPCS with 5028 speckle patterns, each of which corresponds to a timestep in the turbulence. We reduce the spatial resolution to lower the computational cost. We choose 2D slices of the xy plane at $z = 0$ where the 2D flow remains isotropic, and we downsample the 2D slices to 256×256 grids. Each point in the velocity field is averaged with surrounding points before downsampling to avoid aliasing error, which leads to erroneous shift of kinetic energy from small to large scales.

A. Fourier decomposed shear flows within a Fourier band

To employ the theory for uniform shear in multiscale scenarios, we apply Fourier analysis to simulated XPCS to obtain ISF due to scale decomposed shear. For a given discrete velocity field, $\mathbf{u}(\mathbf{x}_i)$, the discrete Fourier transform is given by

$$\hat{\mathbf{u}}(\mathbf{k}) = \sum_{i=0}^{m-1} \mathbf{u}(\mathbf{x}_i) e^{-i\mathbf{k} \cdot \mathbf{x}_i}, \tag{18}$$

where m is the number of indices in the mesh grid, $\mathbf{k} = 2\pi\mathbf{n}/L$ is the Fourier wave number with integer modes $\mathbf{n}$ and domain size L. The Fourier band k is defined as the ceiling value of the wave number magnitude $|\mathbf{k}|$ shown in Fig. 4. We apply Fourier transform to decompose the turbulence scales into Fourier bands at scales k to obtain $\hat{\mathbf{u}}(k)$, and perform inverse Fourier transform (*IFT*) to obtain a velocity field $\mathbf{u}^{(k)}(\mathbf{x}) = \text{IFT}[\hat{\mathbf{u}}(k)]$ in physical space for each Fourier band. In the remaining sections, the notation $|F_S^{(k)}|_{\text{sim}}$ refers to the results from simulated XPCS using the velocity field $\mathbf{u}^{(k)}$, while the notation $|F_S^{(k)}|$ without the subscript sim refers to our derived theoretical equation. The velocity field in a single Fourier mode is sinusoidal, for which the obtained ISF is analogous to the ISF for uniform shear [Eq. (16)] in decaying trend, as described in Appendix A. Note that the two wave numbers k and q represent two independent length scales, where $1/k$ is the scale of velocity fluctuation and $1/q$ is the scale of particle density fluctuation. The $F_S(q, \tau)$ at a fixed q is subject to the shear caused by the flow at all k.

As shown in Fig. 5(a), the $|F_S^{(k)}(\mathbf{q}, \tau)|_{\text{sim}}^2$ in directions of q axis ($\theta = n\pi/2$) oscillates like the squared sinc function in Eq. (16) only at scale $k = 1$, whereas $|F_S^{(k)}(\mathbf{q}, \tau)|_{\text{sim}}^2$ of other scales k [in Fig. 5(b) and 5(c)] mostly damp at a large time delay. The angle θ is counterclockwise from the positive q_x axis in the $q_x q_y$ plane. We notice that the fundamental difference between $k = 1$ and other scales is due to the composition of different Fourier modes. With integer Fourier modes in k_x and k_y, $k = 1$ is the only scale consisting of two pairs of complex conjugates perpendicular to each other in Fourier space (i.e., $k_x = \pm 1$ and $k_y = \pm 1$ in Fig. 4). The two pairs of complex
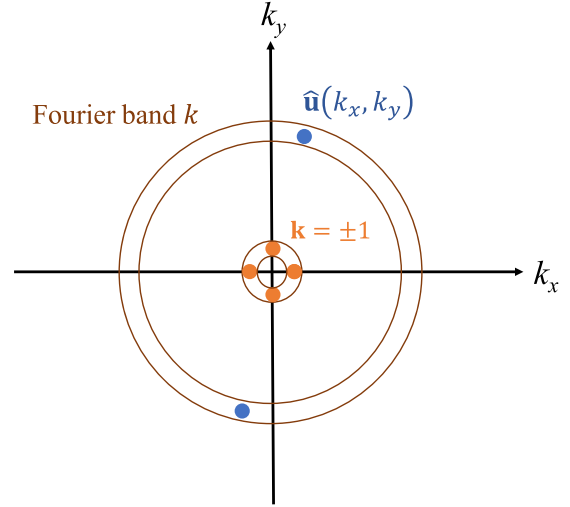

FIG. 4. Schematic of 2D Fourier space. The Fourier band k is defined as the ceiling value of the wave number magnitude $|\mathbf{k}| = \sqrt{k_x^2 + k_y^2}$. In other words, k represents the wave number magnitude encompassed in the brown annulus with unit width. The blue points represent Fourier transformed velocity, $\hat{\mathbf{u}}(k_x, k_y) = \sum_{x=0}^{L} \sum_{y=0}^{L} \mathbf{u}(x, y) \exp[-i(k_x x + k_y y)]$, where two points symmetric about the origin in Fourier space are complex conjugates. For example, the scale $k = 1$ contains only two pairs of complex conjugates (orange points) at $\mathbf{k} = \pm 1$ (i.e., $k_x = \pm 1$ and $k_y = \pm 1$).

conjugates at $k = 1$ represent a flow superimposed by two sinusoidal velocity gradients in perpendicular directions. The velocity gradient in each direction contributes equally to the ISF. Plus $|F_S^{(k)}(\mathbf{q}, \tau)|_{\text{sim}}^2$ in the q axis direction ($\theta = n\pi/2$) is determined by only one component of the velocity due to the dot product in Eq. (14), $|F_S^{(k)}(\mathbf{q}, \tau)|_{\text{sim}}^2$ at $k = 1$ along the q axis is analogous to the uniform shear case discussed in Sec. II C.

To explain the sensitivity of $|F_S^{(k)}(\mathbf{q}, \tau)|_{\text{sim}}^2$ to θ at $k = 1$ in Fig. 5(a), we derive an analytical solution for the superposition of two perpendicular uniform shear flows in Appendix B. In Appendix B, we show that $|F_S(\mathbf{q}, \tau)|^2$ is nearly invariant in any $\mathbf{q}$ direction, and the reduced oscillation for $|F_S(\mathbf{q}, \tau)|^2$ at $\theta \to n\pi/2 + \pi/4$ is analogous to $|F_S^{(k)}(\mathbf{q}, \tau)|_{\text{sim}}^2$ in Fig. 5(a) at $\theta = n\pi/2 + \pi/4$.

For scales of $k > 1$, the Fourier annulus carries more complex conjugate pairs than $k = 1$. In Fig. 5(b) and 5(c), the oscillation of the $|F_S^{(k)}(\mathbf{q}, \tau)|_{\text{sim}}^2$ damps due to the composition of Fourier modes in the Fourier annulus, which leads to superposition of sinusoidal velocity gradients in various orientations in physical space. We seek to approximate the ISF in an annulus at scale $k > 1$ with a function in the form

$$|F_S^{(k)}(q, \tau)| = \exp\left[-\left(v_0^{(k)} q\tau\right)^\alpha\right], \tag{19}$$

where $v_0^{(k)}$ is the characteristic shear velocity at scale k, and α is a constant representing the decay rate. This function is in the form of the Kohlrausch-Williams-Watts (KWW) function, which is a stretched exponential that has been extensively used to approximate the ISF decay due to nonstandard free diffusion such as under phase transition or with heterogeneous dynamics [69–72]. Here the shear component due to
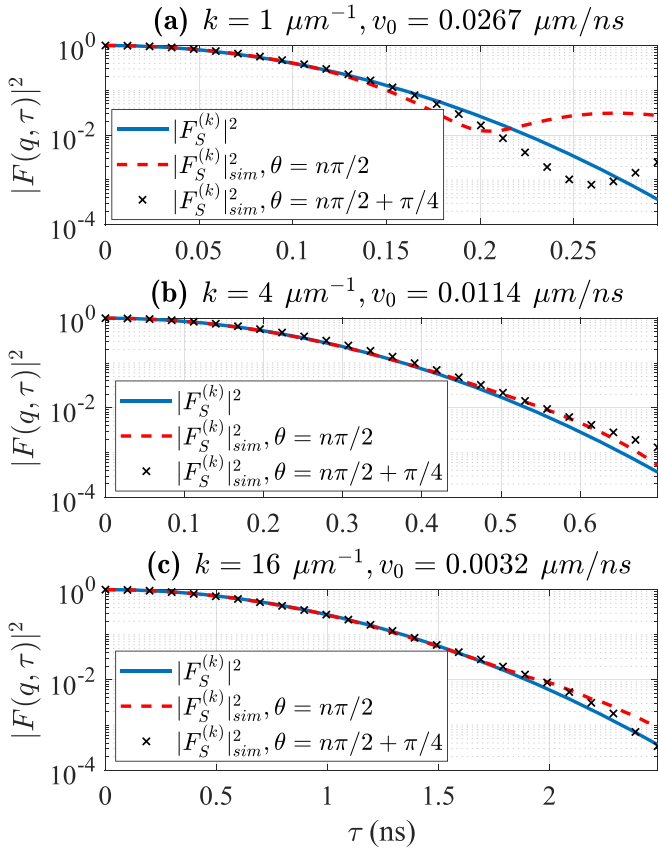
(a) $k = 1 \; \mu m^{-1}, v_0 = 0.0267 \; \mu m/ns$

(b) $k = 4 \; \mu m^{-1}, v_0 = 0.0114 \; \mu m/ns$

(c) $k = 16 \; \mu m^{-1}, v_0 = 0.0032 \; \mu m/ns$

FIG. 5. Comparison of the simulated squared ISF, $|F_S^{(k)}|^2_{\text{sim}}$, for shear at scale k to the analytical equation in Eq. (19), $|F_S^{(k)}|^2 = e^{-2(v_0^{(k)} q\tau)^2}$, approximated using stretched exponential at $q = 0.025 \pm 5 \times 10^{-4}$ Å^{-1}. The oscillation in $|F_S^{(k)}|^2_{\text{sim}}$ at $\theta = n\pi/2$ in the top panel (a) is reduced to approach the analytical equation by changing the orientation of $\mathbf{q}$ (change θ to approach $n\pi/2 + \pi/4$). In (b) and (c), $|F_S^{(k)}|^2_{\text{sim}}$ at any θ follows the analytical equation by incorporating more Fourier modes as k increases. For a multiscale flow, the discrepancy between $|F_S^{(k)}|^2_{\text{sim}}$ and $|F_S^{(k)}|^2$ at scale $k = 1$ is negligible through averaging over θ in q space and collect ISFs at all scales.

multiscale flow is a factor that contributes to the effective diffusion of the particles. With the approximation of the KWW function, the diffusion and shear ISFs [$|F_D(q,\tau)|$ and $|F_S(q,\tau)|$] are both in exponential form. Taking the integer decay rate $\alpha = 2$, one can explicitly derive a timescale at $|F_{\text{general}}| = \exp(-1)$. We fit square of Eq. (19) to the $|F_S^{(k)}(\mathbf{q},\tau)|^2_{\text{sim}}$ and observe good alignment in Fig. 5 except $k = 1$ due to fewer Fourier modes. Even at $k = 1$, the discrepancy between $|F_S^{(k)}(\mathbf{q},\tau)|^2_{\text{sim}}$ and $|F_S^{(k)}(\mathbf{q},\tau)|^2$ [see Fig. 5(a)] is negligible, as we eventually need to average over θ in q space and collect all scales k for multiscale flow.

B. Generalization to multiscale flows

We perform simulated XPCS to Brownian particles in Fourier decomposed flows at each scale k, then $v_0^{(k)}$ is estimated by fitting Eq. (19) to $|F_S^{(k)}(\mathbf{q},\tau)|^2_{\text{sim}}$. The $v_0^{(k)}$ is analogous to the diffusion coefficient D in Eq. (15) that characterizes the rate of particle displacements but due to shear. In isotropic turbulence, the velocity difference $\delta\mathbf{v}$ in

Eq. (14) resulting from shear remains statistically isotropic at each scale [73]. Thus the characteristic shear $v_0^{(k)}$ should remain invariant, which is demonstrated with the invariant $|F_S^{(k)}(q,\tau)|^2_{\text{sim}}$ at different θ for $k > 1$ [see Fig. 5(b) and 5(c)].

Here we show that the multiscale ISF can be written as a product of the ISFs in Eq. (19) for all k. Knowing that the $\mathbf{u}^{(k)}(\mathbf{x})$ is the inverse Fourier transform (IFT) of $\hat{\mathbf{u}}(k)$, and Fourier transform is a linear transformation. The original velocity field can be written as the sum of $\mathbf{u}^{(k)}(\mathbf{x})$ for all k,

$$\mathbf{u}(\mathbf{x}) = \text{IFT}\left(\sum_k \hat{\mathbf{u}}(k)\right) = \sum_k \text{IFT}(\hat{\mathbf{u}}(k)) = \sum_k \mathbf{u}^{(k)}(\mathbf{x}). \quad (20)$$

The $\mathbf{u}^{(k)}(\mathbf{x})$ and $\mathbf{u}^{(k')}(\mathbf{x})$ are uncorrelated if $k \neq k'$ due to the orthogonality of Fourier modes, implying that $\langle \mathbf{u}^{(k)}(\mathbf{x})\mathbf{u}^{(k')}(\mathbf{x})\rangle = \langle \mathbf{u}^{(k)}(\mathbf{x})\rangle\langle \mathbf{u}^{(k')}(\mathbf{x})\rangle$. Replacing $\mathbf{u}^{(k)}$ with $\delta\mathbf{v}^{(k)}$ following the term in Eq. (14) and substituting the sum into the ISF gives,

$$F_S^{\text{multiscale}}(\mathbf{q},\tau) = \frac{1}{N}\sum_j \exp\left\{-i\mathbf{q}\cdot\left[\sum_k \delta\mathbf{v}_j^{(k)}(\mathbf{x})\right]\tau\right\}. \quad (21)$$

Given the condition of uncorrelated velocity fields, the ISF can be written as a product of ISFs for all k. Alternatively, if the shear velocity varies significantly at different length scales (with a steep velocity spectrum), the product also holds true [59],

$$F_S^{\text{multiscale}}(\mathbf{q},\tau) = \prod_k \left\{\frac{1}{N}\sum_j \exp\left[-i\mathbf{q}\cdot\delta\mathbf{v}_j^{(k)}(\mathbf{x})\tau\right]\right\}. \quad (22)$$

Applying the theory for single Fourier band from Eq. (19), it gives a product,

$$\begin{aligned}|F_S^{\text{multiscale}}(q,\tau)| &= \prod_k \left\{\exp\left[-(qv_0^{(k)}\tau)^\alpha\right]\right\} \\ &= \prod_k |F_S^{(k)}(q,\tau)|. \end{aligned} \quad (23)$$

With the product, we start deriving an equation with a stretched exponential for the multiscale ISF using the kinetic energy conservation of Fourier modes. For each scale k, we seek to find the relation between $v_0^{(k)}$ and a root-mean-square (rms) velocity,

$$u_{\text{rms}}^{(k)} = \sqrt{\left\langle\left(u_x^{(k)}\right)^2 + \left(u_y^{(k)}\right)^2\right\rangle}, \quad (24)$$

where $u_x^{(k)}$ and $u_y^{(k)}$ are, respectively, x and y components of Fourier decomposed velocity $\mathbf{u}^{(k)}$. In uniform shear, the ratio between v_0 and rms velocity u_{rms} is strictly constant. For such a flow field with the velocity profile $u(x) = \dot{\gamma}x$ from 0 to L, the ratio is $v_0/u_{\text{rms}} = \sqrt{3}$ by having $v_0 = \dot{\gamma}L$ and $u_{\text{rms}} = (1/\sqrt{3})\dot{\gamma}L$. The $u_{\text{rms}}^{(k)}$ is a typical velocity that represents the square root of the kinetic energy at each scale k. With the orthogonality of Fourier modes [67], the total kinetic energy of the turbulence is the summation of the squared $u_{\text{rms}}^{(k)}$ in all scales,

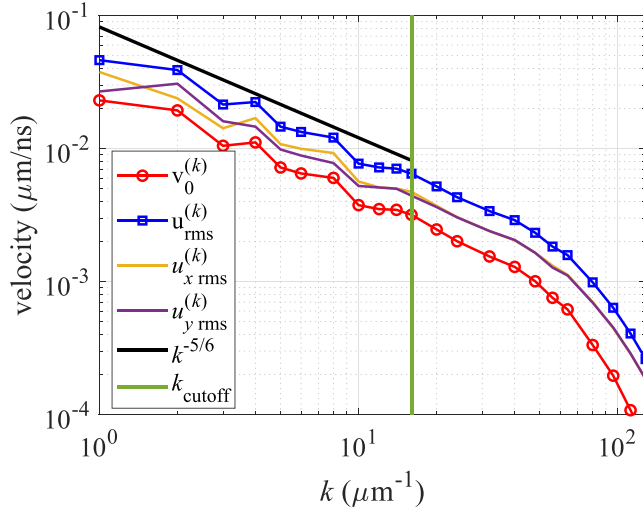$$KE = \frac{1}{2}u_{\text{rms}}^2 = \frac{1}{2}\sum_k \left(u_{\text{rms}}^{(k)}\right)^2. \quad (25)$$

FIG. 6. The characteristic shear velocity, $v_0^{(k)}$, obtained by fitting $|F_S^{(k)}|^2 = e^{-2(v_0^{(k)}q\tau)^2}$ to $|F_S^{(k)}|_{\text{sim}}^2$ for the Fourier decomposed shear at scale k. The $v_0^{(k)}$ scales likewise to the $u_{\text{rms}}^{(k)} = \sqrt{\langle|\mathbf{u}^{(k)}|^2\rangle}$, where $u_{\text{rms}}^{(k)}$ is the square root of the $E^u(k)$ in Fig. 20 following the power law $k^{-5/6}$.

We show that $v_0^{(k)}$ scales likewise to $u_{\text{rms}}^{(k)}$ in Fig. 6 with a power law of $k^{-5/6}$, which is consistent with the scaling of the square root of the turbulence velocity spectrum, $k^{-5/3}$ [67,74]. Since it is known that the kinetic energy conservation of Fourier modes applies to $u_{\text{rms}}^{(k)}$, to apply a similar relation to $v_0^{(k)}$ for later derivation, we demonstrate the linear proportionality between $v_0^{(k)}$ and $u_{\text{rms}}^{(k)}$ by plotting the ratio $c^{(k)} = v_0^{(k)}/u_{\text{rms}}^{(k)}$ and observe a nearly constant value with fluctuation <5% for $k \leqslant 16\,\mu\text{m}^{-1}$ in Fig. 7. However, the ratio decreases beyond the k_{cutoff} (green vertical line in Fig. 7) due to numerical errors of particle velocity interpolation while the scale approaches
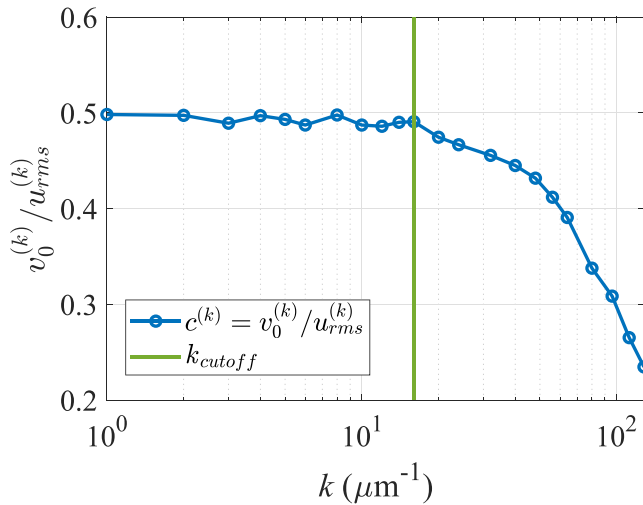
FIG. 7. The ratio $c^{(k)} = v_0^{(k)}/u_{\text{rms}}^{(k)}$ is close to a constant for $k \leqslant k_{\text{cutoff}} = 16\,\mu\text{m}^{-1}$ for the multiscale turbulence, implying that the kinetic energy conversation equation in Eq. (25) applies to $v_0^{(k)}$. The average value of $c^{(k)}$ for $k \leqslant 16\,\mu\text{m}^{-1}$ is 0.492 approximately equal to the ratio obtained for multiscale flow $c^{\text{multiscale}} = 0.490$.
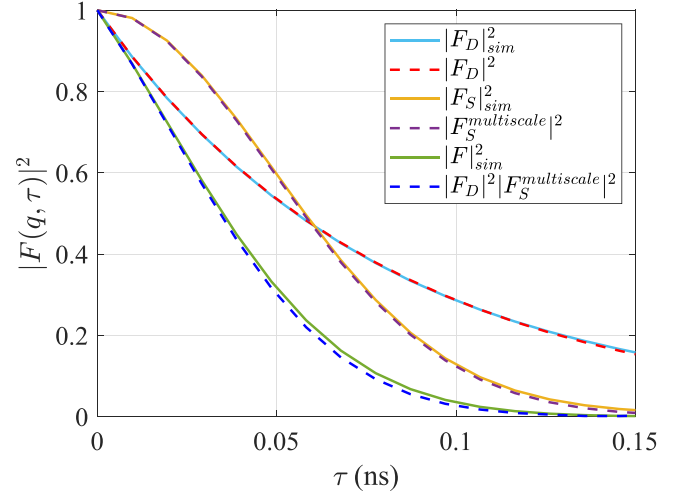

FIG. 8. Validation of analytical equations by comparing $|F(q,\tau)|_{\text{sim}}^2$ for (i) free diffusion to $|F_D(q,\tau)|^2$ in Eq. (15), (ii) multiscale shear to $|F_S^{\text{multiscale}}(q,\tau)|^2$ in Eq. (27), (iii) composition of free diffusion and multiscale shear $|F_{\text{general}}(q,\tau)|^2$ in Eq. (30) with $D = 1 \times 10^{-3}\,cm^2/s$ and $v_0 = 0.042\,\mu\text{m/ns}$ at $q = 0.025 \pm 5 \times 10^{-4}\,\text{Å}^{-1}$.

the grid size. The decay of the ratio mitigates by increasing the mesh resolution where the constant $c^{(k)}$ extends to a larger k seen in Fig. 21 in Appendix D.

Since the $|F_S^{\text{multiscale}}(q,\tau)|$ is the product of the $|F_S^{(k)}(q,\tau)|$ from Eq. (23), it can also be written as,

$$\left|F_S^{\text{multiscale}}(q,\tau)\right| = \exp\left[-\sum_k \left(v_0^{(k)}q\tau\right)^\alpha\right]. \quad (26)$$

For a constant ratio $c^{(k)}$, we expect $v_0^{(k)}$ to follow the energy conservation in Eq. (25), hence, $v_0^2 = \sum_k (v_0^{(k)})^2$. Then the sum in Eq. (26) collapses to a Gaussian function with $\alpha = 2$ analogous to the single-scale theory,

$$|F_S^{\text{multiscale}}(q,\tau)| = \exp[-(v_0q\tau)^2], \quad (27)$$

where the multiscale ISF is validated by fitting it to the simulated ISF for multiscale shear showing good agreement in Fig. 8. In summary, the multiscale ISF is well fitted by the stretched exponential in Eq. (27) if the following conditions are satisfied: Fig. 8(a), multiscale ISF can be presented as a product of ISFs derived for single-scale flows; Fig. 8(b), fitted exponential for single-scale flows with an exponent of $\alpha = 2$; Fig. 8(c), the energy conservation of Fourier modes. From Eqs. (26) and (27), the shear timescale follows relation

$$1/\tau_S^2 = \sum_k \left(1/\tau_S^{(k)}\right)^2, \quad (28)$$

where $\tau_S^{(k)}$ can be obtained at $|F_S^{(k)}| = \exp(-1)$.

By analyzing the simulated XPCS for a multiscale flow without any Fourier scale decomposition, we can obtain a ratio $c^{\text{multiscale}} = v_0/u_{\text{rms}}$. The $c^{\text{multiscale}}$ is expected to be close to c_{avg}, an average of $c^{(k)}$ for $k \leqslant k_{\text{cutoff}}$, illustrated as follows. For that $c^{(k)}$ is nearly invariant for Fourier decomposed flows, the distributive property provides $\sum_k (c^{(k)}u_{\text{rms}}^{(k)})^2 \approx c_{\text{avg}}^2 \sum_k (u_{\text{rms}}^{(k)})^2$. Following Eq. (25), a ratio $c^{\text{multiscale}}$ is
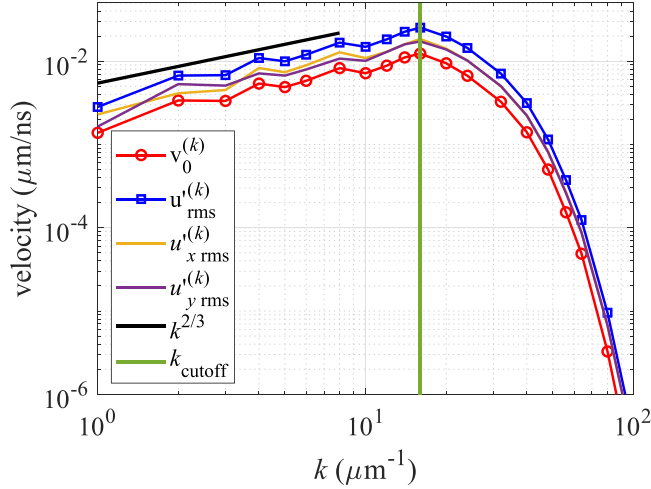
FIG. 9. The characteristic shear velocity, $v_0^{(k)}$, obtained by fitting $|F_S^{(k)}|^2 = e^{-2(v_0^{(k)}q\tau)^2}$ to $|F_S^{(k)}|_{\text{sim}}^2$ for the synthetically modified multiscale flow after Fourier scale decomposition. The modified multiscale flow represents application of instabilities with an increasing velocity spectrum and more energy distributed at small scales near k_{cutoff}. The $v_0^{(k)}$ scales likewise to the $u_{\text{rms}}'^{(k)} = \sqrt{\langle|\mathbf{u}'^{(k)}|^2\rangle}$ where $u_{\text{rms}}'^{(k)}$ is the square root of the $E^{u'}(k)$ in Fig. 22 in Appendix D following the power law $k^{2/3}$.

required to complete

$$(c^{\text{multiscale}})^2 u_{\text{rms}}^2 \approx c_{\text{avg}}^2 \sum_k \left(u_{\text{rms}}^{(k)}\right)^2, \qquad (29)$$

where c_{avg} is an average of $c^{(k)}$ for $k \leqslant k_{\text{cutoff}}$ and, as expected, the $c^{\text{multiscale}} = 0.490$ obtained from the original multiscale turbulence is approximately equal to $c_{\text{avg}} = 0.492$.

When more energy is distributed for $k > k_{\text{cutoff}}$, the accuracy of the fit in Eq. (27) to simulated multiscale ISF becomes slightly lower due to the decrease in the proportionality value $c^{(k)}$. This is because more energetic scales (with larger $v_0^{(k)}$) contribute more to the multiscale ISF. To quantify the impact of the decreasing ratio $c^{(k)}$, we synthetically modify the turbulence flow field to create an increasing velocity spectrum (see Fig. 22 in Appendix D). Instability growth is manifested in the wave number power spectrum through an increasing spectrum at early times when the flow is perturbed at small scales (or energy is injected at small scales due to potential energy release) [75–77]. Small-scale perturbations such as porosity or defects can trigger instability when the target is accelerated, such as due to the passage of a shock. We show that decreasing ratios $c^{(k)}$ due to numerical errors have limited impact on the validity of Eq. (29). The turbulence flow field in Fourier space, $\hat{\mathbf{u}}'$, is modified by multiplying a coefficient, $\hat{\mathbf{u}}' = k^\zeta \hat{\mathbf{u}}$, where $\zeta = 3/2$ for $k \leqslant 16\,\mu\text{m}^{-1}$ and $\zeta = 3/2 - 0.03(k - 16)$ for $k > 16\,\mu\text{m}^{-1}$. The ζ values ensure the peak of the spectrum to be at k_{cutoff} to split roughly equal amount of energy less than and greater than k_{cutoff} in Fig. 9. The velocity spectrum follows a power law of $k^{-5/3+\zeta^2} = k^{4/3}$ for $k \leqslant 16\,\mu\text{m}^{-1}$. Since that the spectral scaling varies between k^1 and k^2 at scales larger than that of the peak in isotropic homogeneous turbulence [78], the $k^{4/3}$ scaling is a reasonable choice as the scaling depends on the initial conditions of the instability. The ratio of

$v_0^{(k)}$ to $u_{\text{rms}}'^{(k)}$ is almost equivalent to a constant $c^{(k)}$ at $k \leqslant k_{\text{cutoff}}$ shown in Fig. 23 in Appendix D. The 54% kinetic energy content beyond the k_{cutoff} brings an absolute error of 4.4% between $c^{\text{multiscale}} = 0.461$ and $c_{\text{avg}} = 0.482$, which imposes limited impact on $|F_S^{\text{multiscale}}(q, \tau)|$.

C. Timescale in multiscale flows

From Eq. (15) and Eq. (27), the diffusion and shear timescales are $\tau_D = 1/Dq^2$ and $\tau_S = 1/v_0q$, respectively. We can measure the two timescales separately only when they differ by orders of magnitude, since the intensity autocorrelation in Eq. (1) only provides the combination of $F_D(q, \tau)$ and $F_S(q, \tau)$ in experiments. While τ_D and τ_S are in the same order of magnitude, it is challenging to extract the diffusion coefficient. This situation is possible in HED conditions with large diffusion coefficient, e.g., $D = 1 \times 10^{-3}\,\text{cm}^2/\text{s}$ employed in this case. At $q = 0.01\,\text{Å}^{-1}$, we get the same timescale $\tau_D = \tau_S = 1\,ns$ with a characteristic shear velocity of 0.01 µm/ns, which is minuscule compared to typical shock velocities in HED experiments [21,79,80].

The product of Eq. (15) and Eq. (27) gives the general ISF,

$$|F_{\text{general}}(q, \tau)| = \exp[-Dq^2\tau - (v_0q\tau)^2], \qquad (30)$$

where we can derive an explicit timescale at $|F_{\text{general}}(q, \tau)| = \exp(-1)$ thanks to the exponential form in both Eq. (15) and Eq. (27),

$$\tau_{\text{general}} = \frac{-Dq^2 + \sqrt{D^2q^4 + 4v_0^2q^2}}{2v_0^2q^2}, \qquad (31)$$

where the timescale is a new contribution but following the properties of the original timescales that the diffusion dominates when $Dq^2 \gg v_0q$, and shear dominates when $Dq^2 \ll v_0q$ [37]. This is demonstrated by observing $\tau \sim 1/q^2$ at $q > 10^{-1}\,\text{Å}^{-1}$ and $\tau \sim 1/q$ at $q < 10^{-2}\,\text{Å}^{-1}$ in Fig. 10. To analyze free diffusion and multiscale shear components, we use Eq. (30) and apply least-squares regression to simulated ISF at various q (equal to or greater than two q values) to fit for D as well as v_0. Alternatively, for a quick but less accurate estimation of D, we can use only two q values to derive an explicit equation,

$$D = \frac{1}{2}\frac{1/\tau_2^2 q_2^2 - 1/\tau_1^2 q_1^2}{1/\tau_2 - 1/\tau_1}, \qquad (32)$$

where τ_1 and τ_2 are the timescales obtained at q_1 and q_2 for $|F_{\text{general}}|^2 = \exp(-1)$. We show the approximation of D using the least-squares regression method in Fig. 11. There is a maximum of approximately $\pm2\%$ timescale error at $|F_{\text{general}}|^2 = \exp(-1)$ between the fitted ISF and the true ISF due to the deviation from the *sinc* function especially at small k. In Fig. 11, the approximation of D is more accurate in the diffusion dominance range or in the range where Dq^2 and v_0q are comparable, while D is sensitive to the timescale change at small q dominated by shear. As opposed to the diffusion coefficient, the characteristic shear velocity v_0 displays more errors at large q due to diffusion dominance in Fig. 12.

The sources of errors in XPCS experiments include photon shot noise, detector noise, partial coherence effect, etc. Under good experimental conditions, the comprehensive impact
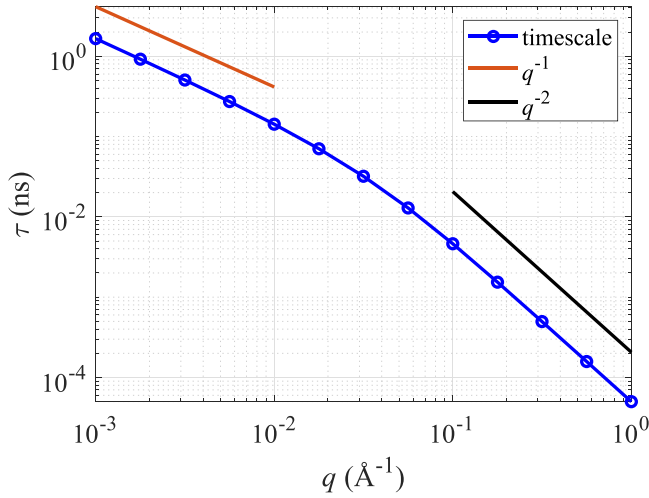
FIG. 10. The timescale for the composition of free diffusion and multiscale shear, τ_{general}, obtained from the multiscale turbulence through the theoretical equation Eq. (30) at $|F_{\text{general}}|^2 = e^{-1}$. The timescale follows q^{-1} at shear dominance ($q \leqslant 10^{-2}\,\text{Å}^{-1}$ for $v_0 = 0.042$ μm/ns) as expected, for that $\tau_S = 1/(\sqrt{2}v_0 q)$ in the shear only case. The timescale follows q^{-2} at diffusion dominance ($q \geqslant 10^{-1}\,\text{Å}^{-1}$ for $D = 1 \times 10^{-3}\,cm^2/s$) as expected, for that $\tau_D = 1/(2D^2 q)$ in the diffusion only case.
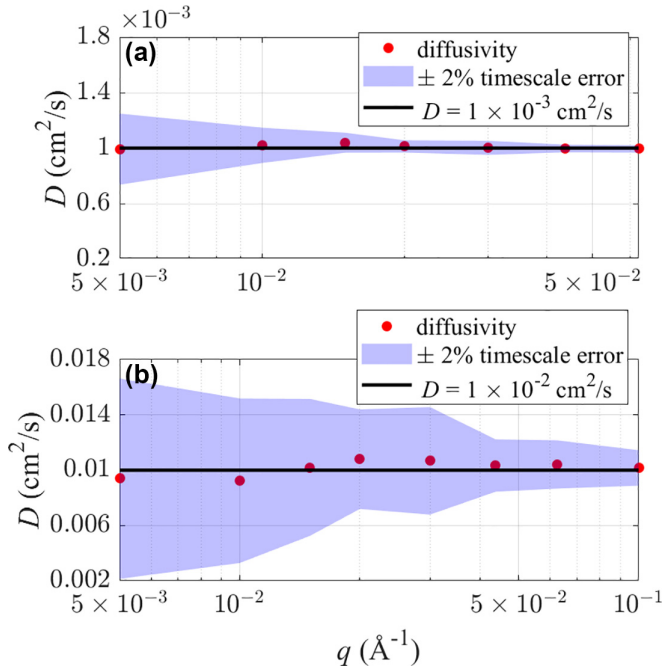
FIG. 11. The diffusion coefficient, D, obtained from the simulated sequential-pulse XPCS using least-squares regression (red dots) compared to the predefined diffusion coefficient (black line) in simulated XPCS. (a) represents the results using the original turbulence and a theoretical $D = 10^{-3}\,cm^2/s$. (b) represents an HED scenario where the turbulence velocity is raised by two orders of magnitude to a few μm/ns and theoretical $D = 10^{-2}\,cm^2/s$. The shaded area is the error of diffusion coefficient with $\pm 2\%$ variation of timescale. The errors in diffusion coefficient estimation is more sensitive to timescale fluctuation at small q ($q \leqslant 10^{-2}\,\text{Å}^{-1}$) due to shear dominance.
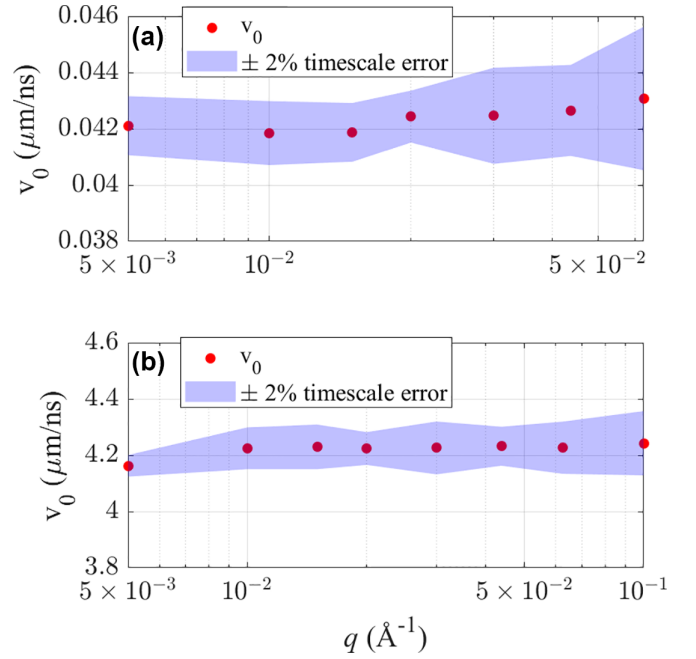

FIG. 12. The characteristic shear velocity, v_0, obtained from the simulated sequential-pulse XPCS using least squares regression. (a) represents the results using the original turbulence and a theoretical $D = 10^{-3}\,cm^2/s$. (b) represents an HED scenario where the turbulence velocity is raised by two orders of magnitude to a few μm/ns and theoretical $D = 10^{-2}\,cm^2/s$. We show that v_0 are consistent by varying q, where the values of v_0 are insignificant for the purpose of this work. The shaded area is the error of characteristic shear velocity with $\pm 2\%$ variation for the timescale, which implies the shear velocity estimation is more sensitive to timescale fluctuation at large q as opposed to the D estimation in Fig. 11.

leads to errors of less than 10% in g_2 or the speckle contrast [81]. In single-pulse mode experiments, more errors are expected due to a lower signal to noise ratio. In two-bunch mode (or split-and-delay) experiments, additional errors can arise from characterizing the pulse intensity ratio and spatial overlap between the pulses. In these cases where XSVS is used, errors are typically between 10%–20% [56,82]. We show an error analysis for Eq. (30) by incorporating typical experimental errors and the $\pm 2\%$ timescale error with fixed average values of D and v_0 in Fig. 13.

Through deriving the general ISF and timescale, our method allows for estimation of diffusion coefficient in the presence of complex multiscale flows, and the maeterial dynamics can be better understood by identifying the individual contribution from free diffusion and isotropic multiscale flows. Our theoretical framework rests on a few important conditions that determine the domain of validity within which we expect it to hold. (i) Isotropy is a weak constraint, as the multiscale ISF requires minor modification for anisotropic shear based on different shear directions. (ii) The theory that separates diffusion and shear is based on different scaling of their timescales. This framework is not applicable if there is any mechanism coupled to diffusion or shear dynamics that changes the scaling of timescale. For example, phase transition can lead to subdiffusion (or superdiffusion) that does
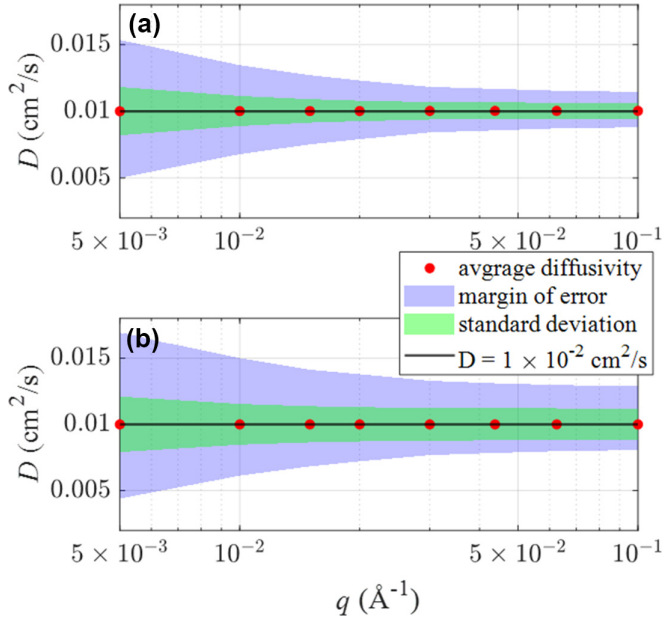
FIG. 13. An error analysis for Eq. (30) by incorporating both typical experimental errors and the $\pm 2\%$ timescale error with fixed average values of $D = 1 \times 10^{-2}\,cm^2/s$ and $v_0 = 4.2$ µm/ns. For the experimental errors, we add either (a) $\pm 10\%$ or (b) $\pm 20\%$ variation on $|F_{general}|^2$.

not follow a standard mean-squared-displacement theory. (iii) In the ISF in Eq. (14), it is assumed that the shear velocity is quasisteady over the temporal resolution of the diagnostic, τ. The framework could break down if the diagnostic has a relatively coarse temporal resolution that cannot resolve rapid changes in shear. As for example applications, our framework works for two-fluid mixing, and microdroplet formation as long as droplets remain much smaller than the probe volume. However, it may break down for reactive systems, where altered timescale scaling can invalidate the theory.

Finding diffusion coefficient D is relevant to explore material viscosity η through the Stokes-Einstein relationship [83], $D = k_B T / 6\pi \eta a$, where a is the particle radius. A typical diameter of nanoparticles used in experiments is around a hundred nanometers [84]. This relationship holds true with the assumption of Stokes law at low Reynolds number. In our study, the Reynolds number remains low near the length scale of particle diameter, whereas high Reynolds number exists globally with the presence of multiscale flow and turbulence. However, further investigation is required to accurately approximate η in future studies.

IV. PROBING ULTRAFAST DYNAMICS USING XSVS

A. Single-pulse XSVS

To explore the diffusivity and viscosity in warm dense matter under shock compression, it is required to access material dynamics below nanosecond timescale. This is hardly accessible with sequential x-ray pulses, while the frame rate of state-of-the-art detectors is limited for XPCS to probe down to submicrosecond timescale [85]. One method of accessing fast dynamics is through single-pulse mode [23] (with timescale
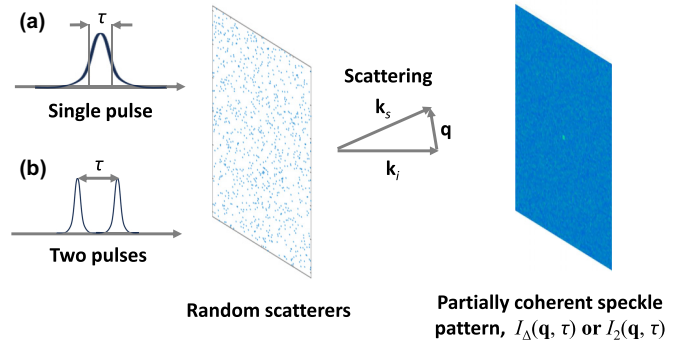

FIG. 14. Schematics of (a) single-pulse scattering where the intensity distribution, $I_\Delta(\mathbf{q}, \tau)$, is the scattering intensity integrated over the x-ray pulse duration τ, and (b) double-pulse scattering where the intensity distribution, $I_2(\mathbf{q}, \tau)$, is the sum of the scattering intensity from the two pulses separated by τ. The scattering intensity generated by both methods are typically analyzed using XSVS.

of 100-femtosecond regime), where single-pulse XSVS is used to analyze the contrast as a function of the exposure time over the x-ray pulse duration [24–26] shown in Fig. 14. Single-pulse XSVS is conducted by varying the x-ray pulse duration instead of the separation time between pulses, since the acquisition time of current detectors is much larger than the x-ray pulse time in tens of femtoseconds.

For single-pulse scattering, we can model a single incoherent speckle pattern by superimposing the scattering intensities from M statistically independent coherent speckle patterns. The probability distribution of the normalized intensity follows the Erlang distribution,

$$P_M(\kappa) = \frac{M^M \kappa^{M-1}}{(M-1)!} \exp(-\kappa M), \qquad (33)$$

where $M = 1/\beta(q)$ and $\kappa(q) = I(q)/\langle I(q)\rangle$. For $M = 1$, the probability distribution follows an exponential form implying the pattern mostly consists of grainy speckles. For $M > 1$, the incoherent speckle pattern leads to decreased contrast, hence the peak of the probability distribution $P_M(\kappa)$ shifts toward a diffused speckle pattern, $\kappa(q) = 1$, as shown in Fig. 15. In our simulated scattering, coherent illumination is assumed with $M = 1$.

In single-pulse scattering, the intensity, $I_\Delta(q, \tau)$, records the integrated signal over the pulse duration τ,

$$I_\Delta(q, \tau) = \int_0^\tau I(q, t)dt. \qquad (34)$$

The speckle visibility is specified by the contrast of single-pulse XSVS, β_Δ, which has the same definition as in Eq. (3) by replacing $I(q, t)$ with $I_\Delta(q, \tau)$. In simulated single-pulse scattering, the integrated intensity is obtained by superimposing all speckle patterns generated within the time duration τ.

From the Siegert relation in Eq. (2), the contrast can be written as an integration of the squared ISF over the x-ray pulse time [53,86],

$$\beta_\Delta(q, \tau) = \beta_0(q) \int_0^\tau 2(1 - t/\tau)|F(q, t)|^2 dt/\tau^2, \qquad (35)$$
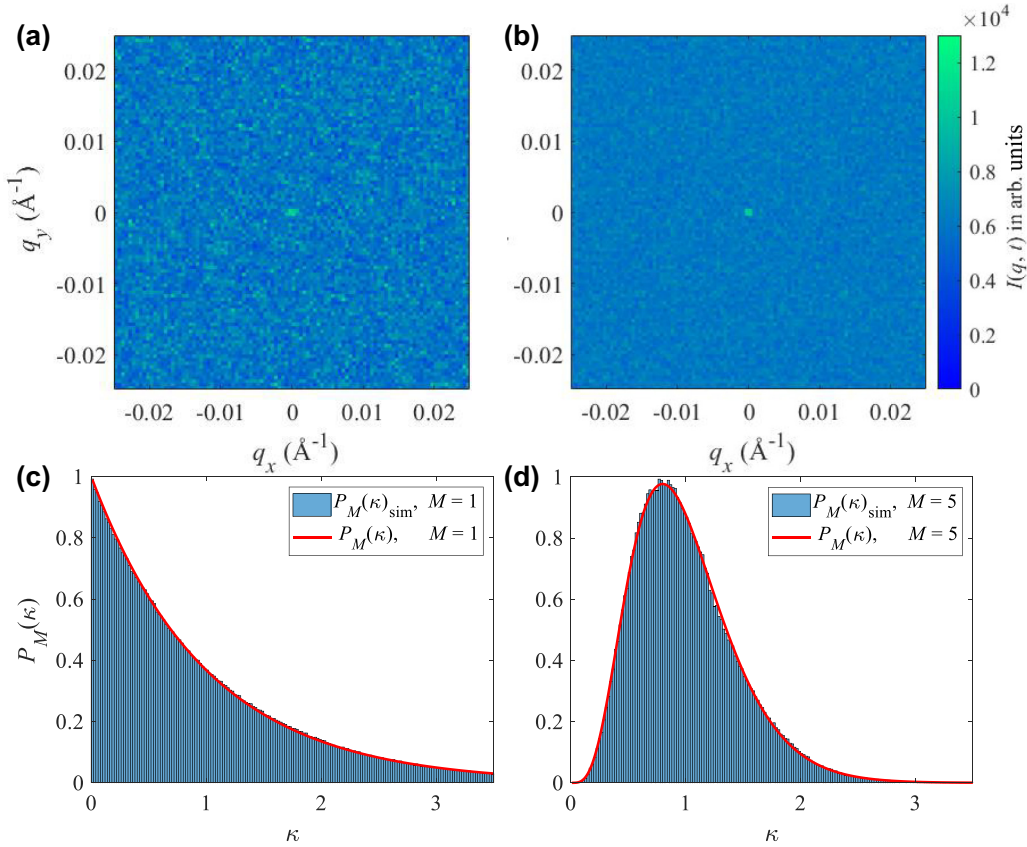
FIG. 15. (a) A coherent speckle pattern with (c) the probability distribution of the normalized intensity, $\kappa(q) = I_\Delta(q)/\langle I_\Delta(q) \rangle$, in the shape of an exponential decay. (b) A partially coherent speckle pattern by superimposing five independent speckle patterns (no correlation with sufficiently large time delay), which results in diffused intensity distribution and (d) the peak of the probability distribution shifts toward the averaged intensity, $\kappa = 1$.

where $\beta_0(q)$ is obtained for the normalized intensity variation with minimal pulse duration, represented by a single speckle pattern without superposition in simulated single-pulse scattering.

Substituting Eq. (30) and taking the definite integral, the contrast decay gives

$$\beta_\Delta(q, \tau) = \beta_0(q) \left\{ \left(\frac{2V\tau + G}{V\tau^2} \right) \int_0^\tau e^{-2Vt^2 - 2Gt} dt \right.$$

$$\left. + \frac{e^{-2V\tau^2 - 2G\tau} - 1}{2V\tau^2} \right\}, \tag{36}$$

where $G = Dq^2$ and $V = (v_0 q)^2$. We validate this theoretical equation through simulating single-pulse scattering by integrating the intensity on discrete speckle patterns over the pulse time, where the theoretical contrasts agree with the simulated contrasts from single-pulse XSVS in Fig. 16. Note that the equation contains a definite integral that can be calculated numerically, since a complete analytical solution contains error functions leading to extra numerical errors shown in Appendix C. Estimation of D and v_0 can be obtained through least-squares regression with the input arguments q, β_0, τ, and β_Δ. In Figs. 25 and 26 in Appendix D, the approximated D and v_0 resemble the ones with sequential-pulse XPCS as described in Sec. III C. The errors in the estimation of D

and v_0 are relatively large compared to the sequential-pulse XPCS for that more numerical errors are introduced by integrating discrete intensity distribution over the pulse time. It is difficult to define an identical timescale to the sequential-pulse XPCS since the exponential function is embedded in the definite integral. However, we can characterize the contrast decay time as a timescale for τ at $\beta_\Delta = \exp(-1)$ that still follows the scaling of diffusion and shear in q space shown in Fig. 17.

B. Double-pulse XSVS

Double-pulse XSVS is a method for analyzing the contrast as a function of the time separation between two short x-ray pulses. To capture ultrafast dynamics, the time separation between pulses requires to be short, so the detector only records the sum of the scattering patterns with limited integration time. For single-pulse experiments, the pulse time is limited up to the order of several hundreds of femtoseconds to avoid perturbing the system with excessive radiation. Due to the nature of the double-pulse structure, XSVS can be used to analyze dynamics with a broader timescale operated between picoseconds using the split-and-delay method by splitting an individual pulse into two through optical approaches [56,87] and nanoseconds using two-bunch mode [88,89].
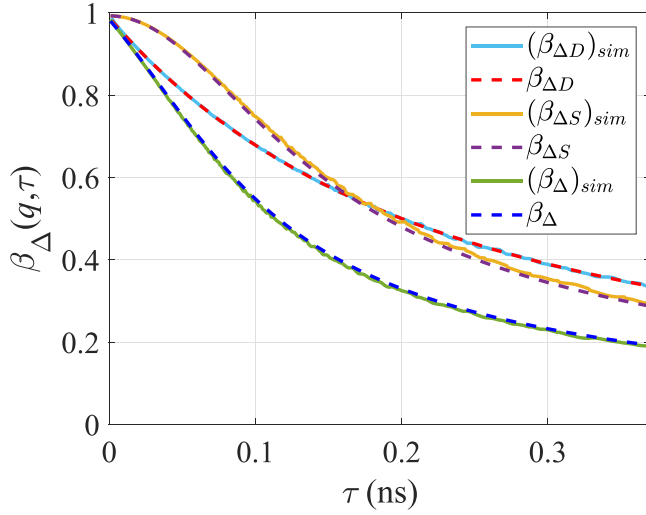
FIG. 16. Validation of theoretical contrast by comparing simulated optical contrast, $(\beta_\Delta)_{\text{sim}}(q, \tau)$, in single-pulse XSVS for (i) free diffusion to $\beta_{\Delta D}(q, \tau)$ in Eq. (C1), (ii) multiscale shear to $\beta_{\Delta S}(q, \tau)$ in Eq. (C2), (iii) composition of free diffusion and multiscale shear to $\beta_\Delta(q, \tau)$ in Eq. (36) with $D = 1 \times 10^{-3}\ cm^2/s$ and $v_0 = 0.042\ \mu m/ns$ at $q = 0.025 \pm 5 \times 10^{-4}\ \text{Å}^{-1}$.

In double-pulse scattering, the scattering pattern records the summed scattering intensity, $I_2(q, \tau) = I(q, t) + I(q, t + \tau)$ with a time separation τ between the two pulses. With two x-ray pulses of identical intensity, the contrast is derived [90] from the Siegert relation,

$$\beta_2(q, \tau) = \tfrac{1}{2}\beta_0(q)(1 + |F(q, \tau)|^2). \quad (37)$$

The simulated double-pulse scattering is performed through superimposing every two scattering patterns separated by τ,
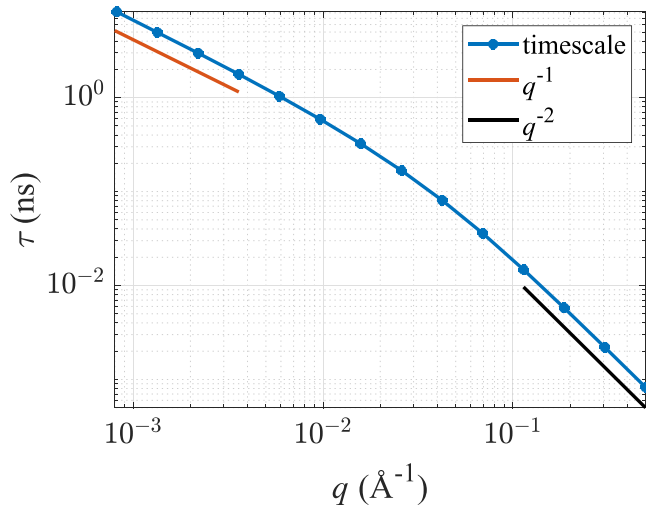
FIG. 17. The timescale for single-pulse XSVS with the composition of free diffusion and multiscale shear, τ_{general}, obtained through the multiscale turbulence using theoretical equation, Eq. (36), at $\beta_\Delta = e^{-1}$. The timescale still follows q^{-1} at shear dominance ($q \leqslant 10^{-2}\ \text{Å}^{-1}$) and q^{-2} at diffusion dominance ($q \geqslant 10^{-1}\ \text{Å}^{-1}$) even though the timescale with the integration of $|F(q, \tau)^2|$ is different from that of in Fig. 10.
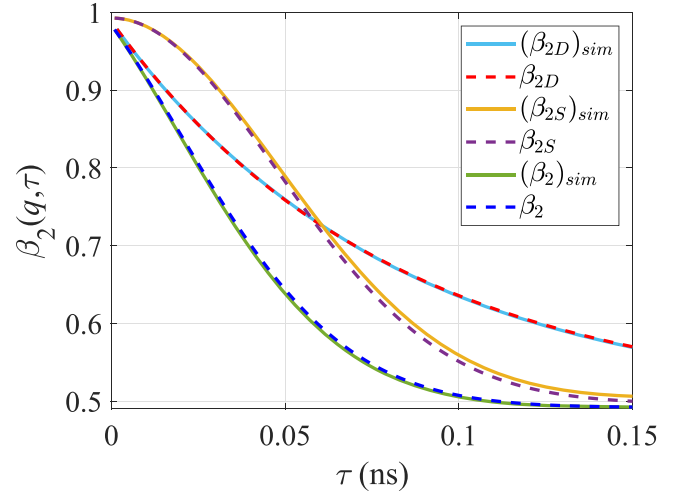

FIG. 18. Validation of theoretical contrast by comparing simulated optical contrast, $(\beta_2)_{\text{sim}}(\mathbf{q}, \tau)$, in double-pulse XSVS for (i) free diffusion to $\beta_{2D}(q, \tau)$ using Eqs. (37) and (15), (ii) multiscale shear to $\beta_{2S}(q, \tau)$ using Eqs. (37) and (27), (iii) composition of free diffusion and multiscale shear to $\beta_2(q, \tau)$ using Eqs. (37) and (30) with $D = 1 \times 10^{-3}\ \text{cm}^2/s$ and $v_0 = 0.042\ \mu m/ns$ at $q = 0.025 \pm 5 \times 10^{-4}\ \text{Å}^{-1}$.

in which β_0 is the contrast for a speckle pattern at $\tau = 0$ assumed to be completely coherent. Note that the contrast in double-pulse XSVS has an asymptotic limit of $\beta_0/2$ for $\tau \to \infty$ instead of zero in sequential-pulse XPCS [Eq. (30)] and single-pulse XSVS [Eq. (36)]. With the asymptotic limit, β is more sensitive to contrast fluctuation, which might lead to extra errors while estimating D and v_0. The comparison in Fig. 18 shows good agreement between the theoretical contrasts and the simulated contrasts from the double-pulse XSVS. Since Eq. (37) directly incorporates the Siegert relation, the timescales remain identical to the sequential-pulse XPCS in Eq. (31) (see Fig. 10). We can apply either Eq. (32) or least-squares regression to approximate D and v_0, which resembles the estimation in sequential-pulse XPCS in Figs. 27 and 28 in Appendix D.

Although the pulse structures from single-pulse mode and two-bunch mode (or split-and-delay method) offer the capability for measurements below nanosecond timescale, q-range limit imposes difficulties on reaching the minimum timescale possible to neglect shear effects on ISF by having diffusion dominance. At high q range, the photon flux is significantly reduced, meanwhile, decreased contrast and low photons per pixel lead to a low signal-to-noise ratio [91,92]. Thus more repetitions are required to improve the results to follow the photon statistics at high q. Additionally, scattering of plasma at high q imposes risks on shifting photon energy and broadening energy bandwidth due to inelastic scattering by transferring more momentum to free electrons. For these reasons, developing such a methodology for diffusion characterization at an working range of intermediate q range, where the ISF is determined by both free diffusion and multiscale shear, is essential for future experiments in warm dense matter with fast dynamics.

V. CONCLUDING REMARKS

In this study, we have developed a comprehensive theoretical framework for XPCS, deriving the ISF for samples undergoing isotropic multiscale shear flows. Our approach leverages Fourier analysis to decompose multiscale flows into components within Fourier bands, allowing characterization of the interplay between shear and free diffusion in simulated XPCS based on single-scale theory. By extending the theory of a uniform shear flow to multiscales, we have introduced a general timescale that accounts for the complex dynamics through conserved energy in Fourier decomposition and a stretched exponential approximation to the ISF.

We demonstrate that the combination of multiscale shear and free diffusion can be effectively analyzed in sequential-pulse XPCS, single-pulse XSVS, and double-pulse XSVS techniques. These experimental techniques support the versatility of our theoretical framework over timescales ranging from picoseconds to hours. Our simulated results validated the theoretical models, showing that the diffusion coefficient and characteristic shear velocity can be measured, even with comparable associated timescales.

Our analysis highlights the significance of understanding the dependence of different physical processes on q using a general timescale. For measurement of diffusion coefficient and multiscale shear velocity, it is no longer crucial to distinguish the individual contribution of shear and diffusion using two separate timescales. This relaxes the limitation to high q range to maintain diffusion dominance in future experiments, where the photon flux and contrast are considerably reduced. This is important for advancing the application of XPCS in studying material properties incurring fast dynamics when shear flows are prominent, such as in high-energy-density shock-induced multiscale flows. We hope the methodologies presented here can help relax the restriction to a particular q range that avoids shear effects in designing more sophisticated experiments and in developing new analytical tools for probing the dynamics in multiscale flows.

DATA AVAILABILITY

The data that support the findings of this article are not publicly available upon publication because it is not technically feasible and/or the cost of preparing, depositing, and hosting the data would be prohibitive within the terms of this research project. The data are available from the authors upon reasonable request.

APPENDIX A: ISF FOR SINGLE-SCALE SINUSOIDAL FLOW

In Sec. II B, we discuss the analytical solution of ISF for uniform shear, whereas the flow profiles obtained from Fourier analysis are sinusoids. To demonstrate the resemblance between these two cases, we find $|F_S(q, \tau)|^2$ for a sinusoidal velocity difference, $\delta v(y) = u_0[\sin(y_2) - \sin(y_1)]$, with constant velocity u_0. Substituting the velocity difference into the last term of Eq. (14) and integrate over the field size,

$$|F_S(q, \tau)|^2 = \frac{1}{L^2} \int_0^L \int_0^L \exp[iqu_0[\sin(x_2) - \sin(x_1)]\tau]$$
$$\times \, dx_1 dx_2. \tag{A1}$$

We are not aware of a closed form solution for this integral, but we can approximate the solution using an asymptotic expansion. The function $\exp[iqu_0\sin(x)\tau]$ can be expanded involving Bessel functions of the first kind according to the Jacobi-Anger expansion,

$$e^{iq\tau u_0 \sin(x)} = \sum_{n=-\infty}^{\infty} J_n(q\tau u_0)e^{inx}. \tag{A2}$$

Substituting this series into one of the integrals we derive,

$$\int_0^L e^{iq\tau u_0 \sin(x)}dx = \sum_{n=-\infty}^{\infty} \left[J_n(q\tau u_0) \int_0^L e^{inx}dx \right]. \tag{A3}$$
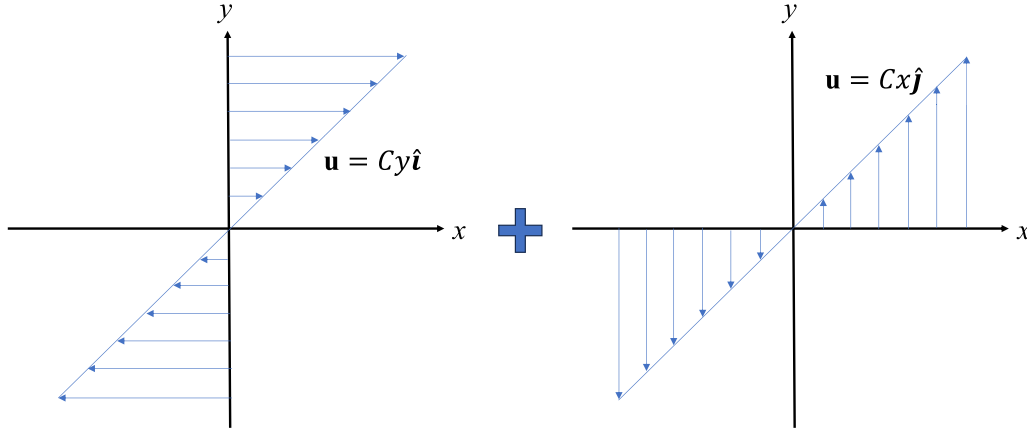
FIG. 19. Schematic of superimposing two perpendicular uniform shear flows, $\mathbf{u} = Cy\hat{\mathbf{i}}$ and $\mathbf{u} = Cx\hat{\mathbf{j}}$, where C is a constant rate of shear.

The integral $\int_0^L e^{\text{inx}} dx = L$ for $n = 0$, and $\int_0^L e^{\text{inx}} dx = [\exp(inL) - 1]/in$ for $n \neq 0$. Taking the domain size $L = 2\pi$, the integral vanishes for $n \neq 0$, hence, the asymptotic expansion of $|F_S(q, \tau)|^2$ becomes

$$|F_S(q, \tau)|^2 = \frac{1}{L^2} J_0^2(q\tau u_0) L^2 = J_0^2(q\tau u_0), \qquad \text{(A4)}$$

which displays similar trend of decay as compared to $\sin^2(q\tau v_0)/(q\tau v_0)^2$. It approaches the stretched exponential approximation with reduced oscillation using the superposition method discussed in Appendix B.

APPENDIX B: SUPERPOSITION OF SHEAR IN PERPENDICULAR DIRECTIONS

In Sec. II B, we discuss the analytical solution of ISF for uniform shear with the flow velocity in the direction of the x axis. Here we superimpose a shear flow field of the same magnitude but with velocity oriented in the y axis (see Fig. 19) to demonstrate the nearly invariance of $|F_S(\mathbf{q}, \tau)|^2$ as a function of $\mathbf{q}$ proportional to the angle θ.

From Eq. (14), the ISF for shear is written as

$$F_S(\mathbf{q}, \tau) = \frac{1}{N} \sum_j e^{-i\mathbf{q} \cdot \delta \mathbf{v}_j \tau}, \qquad \text{(B1)}$$

where we can decompose the vectors $\mathbf{q} = \mathbf{q}_x + \mathbf{q}_y$ and $\delta \mathbf{v}_j = \delta \mathbf{v}_{jx} + \delta \mathbf{v}_{jy}$ in 2D Cartesian coordinate, and the squared ISF is given by,

$$|F_S(\mathbf{q}, \tau)|^2 = \frac{1}{N^2} \left| \sum_j \sum_l e^{-i[q_x(\delta v_{jx} - \delta v_{lx}) + q_y(\delta v_{jy} - \delta v_{ly})]\tau} \right|, \qquad \text{(B2)}$$

then the velocity difference due to shear can be represented by $\delta v_x = \dot{\gamma}_x(y_1 - y_2)$ and $\delta v_y = \dot{\gamma}_y(x_1 - x_2)$. Replacing the sum with an integral over the field size,

$$|F_S(\mathbf{q}, \tau)|^2 = \frac{1}{L^2} \int_{-L/2}^{L/2} \int_{-L/2}^{L/2} \exp[iq_x \dot{\gamma}_x (y_2 - y_1)\tau] dy_1 dy_2$$
$$\times \frac{1}{L^2} \int_{-L/2}^{L/2} \int_{-L/2}^{L/2} \exp[iq_y \dot{\gamma}_y (x_2 - x_1)\tau] dx_1 dx_2$$

$$= \frac{1}{L^4} \left[\frac{\exp(iq_x \dot{\gamma}_x y_2 \tau)}{iq_x \dot{\gamma}_x \tau} \right]_{-L/2}^{L/2} \left[\frac{\exp(-iq_x \dot{\gamma}_x y_1 \tau)}{-iq_x \dot{\gamma}_x \tau} \right]_{-L/2}^{L/2}$$
$$\times \left[\frac{\exp(iq_y \dot{\gamma}_y x_2 \tau)}{iq_y \dot{\gamma}_y \tau} \right]_{-L/2}^{L/2} \left[\frac{\exp(-iq_y \dot{\gamma}_y x_1 \tau)}{-iq_y \dot{\gamma}_y \tau} \right]_{-L/2}^{L/2}. \qquad \text{(B3)}$$

Applying the Euler formula after integration and define the characteristic shear velocity $v_0 = \dot{\gamma}_x L = \dot{\gamma}_y L$ for the same magnitude of uniform shear but in perpendicular directions,

$$|F_S(\mathbf{q}, \tau)|^2 = \frac{\sin^2(v_0 q_x \tau/2)}{(v_0 q_x \tau/2)^2} \frac{\sin^2(v_0 q_y \tau/2)}{(v_0 q_y \tau/2)^2}, \qquad \text{(B4)}$$

where $q_x = q \cos\theta$ and $q_y = q \sin\theta$. This equation manifests similar values at any θ as expected for a nearly invariant $|F_S(\mathbf{q}, \tau)|^2$ at a fixed q, and approaches Eq. (16) for $\theta \to n\pi/2$. The oscillation in $|F_S(\mathbf{q}, \tau)|^2$ is reduced and approaches a Gaussian shape for $\theta \to n\pi/2 + \pi/4$. Note that the ISF
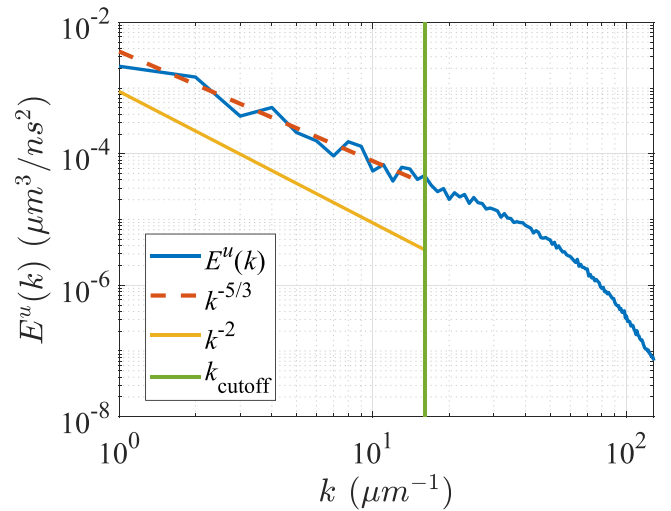
FIG. 20. Spectra of velocity, $E^u(k)$, for the multiscale flow follwoing the Kolmogorov's $k^{-5/3}$ power law. Here $E^u(k) = \sum_{||\mathbf{k}| - k| < 0.5} \frac{1}{2} |\hat{\mathbf{u}}(\mathbf{k})|^2$, where $\hat{\mathbf{u}}(\mathbf{k})$ is the Fourier coefficient. The numerical errors in multiscale theory due to particle velocity interpolation near mesh grid size is negligible for $k \leqslant k_{\text{cutoff}} = 16\,\mu\text{m}^{-1}$.
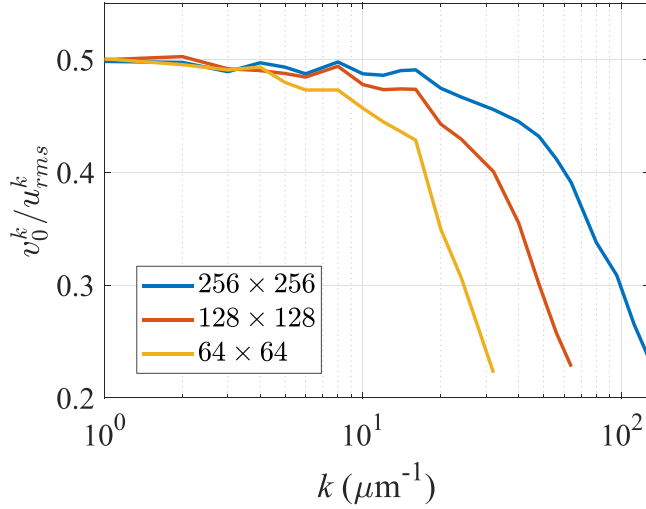
FIG. 21. The ratio $c^{(k)} = v_0^{(k)}/u_{\mathrm{rms}}^{(k)}$ for three mesh resolutions. Higher resolution extends the constant ratio to a smaller length scale. The decreasing ratio has limited impact on the multiscale theory even with more energy weighted at small scales.

only tracks the particle velocity difference, therefore the orientation of the perpendicular flows does not affect the result. That said, the rotation only velocity field (solid body rotation), $\mathbf{u} = C(-y\hat{\mathbf{i}} + x\hat{\mathbf{j}})$, and the strain-only velocity field $\mathbf{u} = C(y\hat{\mathbf{i}} + x\hat{\mathbf{j}})$, with a constant C, lead to identical $|F_S(\mathbf{q}, \tau)|^2$.

APPENDIX C: ANALYTICAL CONTRAST FOR SINGLE-PULSE XSVS

Analytical solution of contrast for single-pulse XSVS differs from sequential-pulse XPCS and double-pulse XSVS as an integral over the x-ray pulse delay is required to incorporate
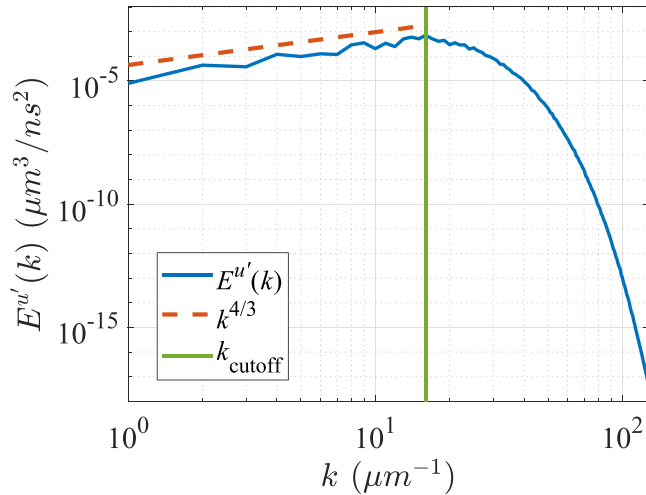

FIG. 22. Spectra of velocity, $E^{u'}(k) = \sum_{||\mathbf{k}|-k|<0.5} \frac{1}{2}|\hat{\mathbf{u}}'(\mathbf{k})|^2$, for the modified multiscale flow. Here $\hat{\mathbf{u}}' = k^{\zeta}\hat{\mathbf{u}}$, where $\zeta = 3/2$ for $k \leqslant 16\,\mu\mathrm{m}^{-1}$ and $\zeta = 3/2 - 0.03(k - 16)$ for $k > 16\,\mu\mathrm{m}^{-1}$. This represents the case like instabilities with more kinetic energy at small scales to verify the limited impact of small-scale energy on the multiscale theory. The spectrum follows a power law of $k^{4/3} = k^{-5/3+\zeta^2}$ for $k \leqslant 16\,\mu\mathrm{m}^{-1}$.
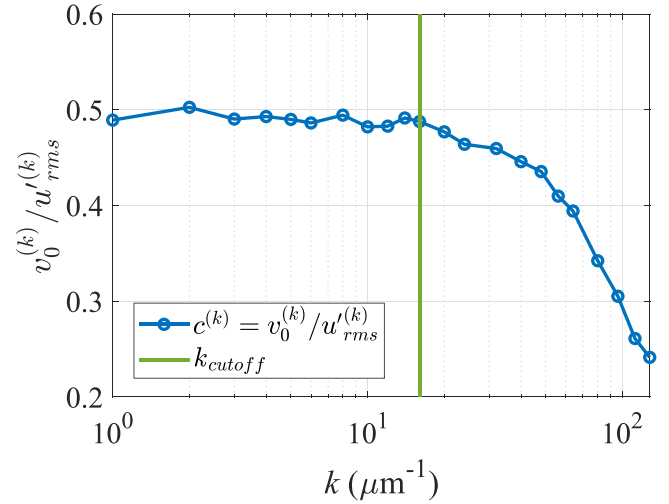

FIG. 23. The ratio $c^{(k)} = v_0^{(k)}/u_{\mathrm{rms}}^{\prime(k)}$ is approximately a constant for $k \leqslant 16\,\mu\mathrm{m}^{-1} = k_{\mathrm{cutoff}}$ for the synthetically modified multiscale flow, implying a nearly linear scaling between v_0 and $u_{\mathrm{rms}}^{\prime(k)}$.

$|F(q, \tau)|^2$ in the contrast function in Eq. (35). The contrast for free diffusion has been used extensively [25,53] by substituting Eq. (15) into Eq. (35),

$$\beta_{\Delta D}(q, \tau) = \beta_0(q)\left[\frac{\exp(-2Dq^2\tau) - 1 + 2Dq^2\tau}{2(Dq^2\tau)^2}\right]. \quad (C1)$$

Similarly, we substitute the $|F_S^{\mathrm{multiscale}}(q, \tau)|^2$ for multiscale shear in Eq. (27) into Eq. (35) with the stretched exponential
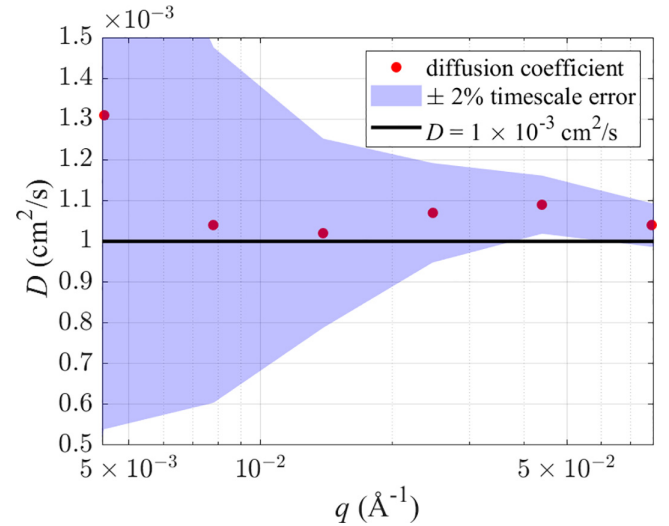
FIG. 24. The diffusion coefficient, D, obtained from the simulated XPCS using explicit formula in Eq. (32) (red dots) compared to the predefined diffusion coefficient (black line). The shaded area is the error of diffusion coefficient with $\pm 2\%$ variation for the timescale implying the diffusion coefficient estimation is more sensitive to timescale fluctuation at small q. The explicit equation is a convenient way to estimate D using two q values, however, it introduces more errors compared to that of the least-squares regression method in Fig. 11(a).

FIG. 25. The diffusion coefficient, D, obtained from the simulated single-pulse XSVS using least-squares regression (red dots) compared to the predefined diffusion coefficient (black line). The shaded errors are larger than that of sequential-pulse XPCS [Fig. 11(a)] and double-pulse XSVS (Fig. 27) due to integration over discrete speckle patterns in time.

approximation, to derive the contrast function,

$$\beta_{\Delta S}(q, \tau)$$
$$= \beta_0(q) \left[\frac{e^{-2(v_0 q \tau)^2} - 1 + \sqrt{2\pi}(v_0 q \tau) \mathrm{erf}(\sqrt{2} v_0 q \tau)}{2(v_0 q \tau)^2} \right]. \tag{C2}$$

We describe the contrast that consists of both free diffusion and multiscale shear by substituting Eq. (30) into Eq. (35) in Sec. IV A. One can further simplify the numerical integral in

FIG. 26. The characteristic shear velocity, v_0, obtained from the simulated single-pulse XSVS using least-squares regression. The shaded errors are larger than that of sequential-pulse XPCS [Fig. 12(a)] and double-pulse XSVS (Fig. 28) due to integration over discrete speckle patterns in time.
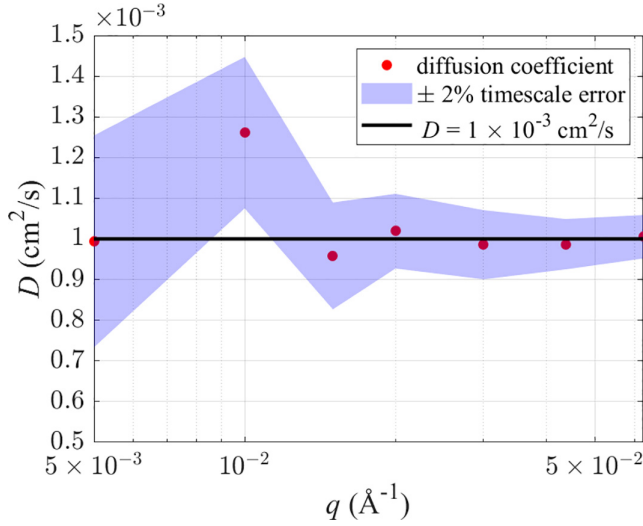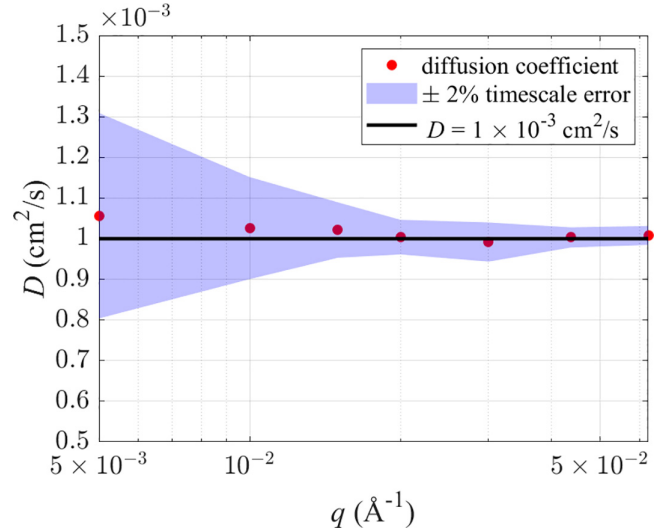

FIG. 27. The diffusion coefficient, D, obtained from the simulated double-pulse XSVS using least-squares regression (red dots) compared to the predefined diffusion coefficient (black line). The shaded errors are comparable to that of sequential-pulse XPCS [Fig. 11(a)] by having direct proportionality between contrast and $|F(q, \tau)|^2$.

Eq. (36) to achieve an analytical solution with the erf function,

$$\beta_\Delta(q, \tau)$$
$$= \beta_0(q) \left\{ \frac{\sqrt{\pi}(2V\tau + G) e^{\frac{G^2}{2V}} \left[\mathrm{erf}\left(\frac{2V\tau + G}{\sqrt{2V}}\right) - \mathrm{erf}\left(\frac{G}{\sqrt{2V}}\right) \right]}{(2V)^{3/2} \tau^2} \right.$$
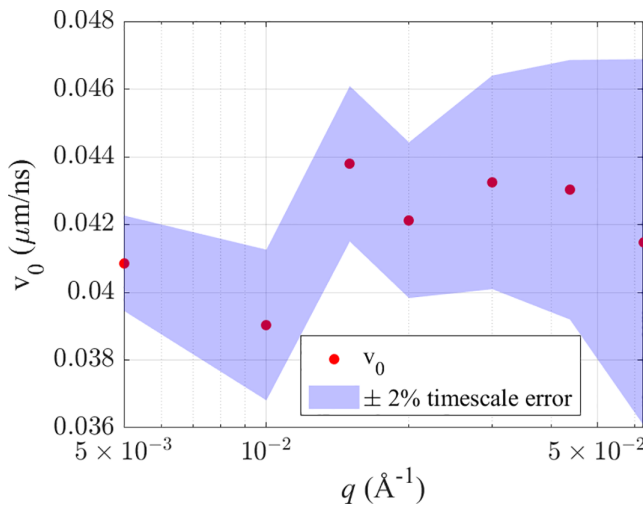$$\left. + \frac{e^{-2V\tau^2 - 2G\tau} - 1}{2V\tau^2} \right\}, \tag{C3}$$
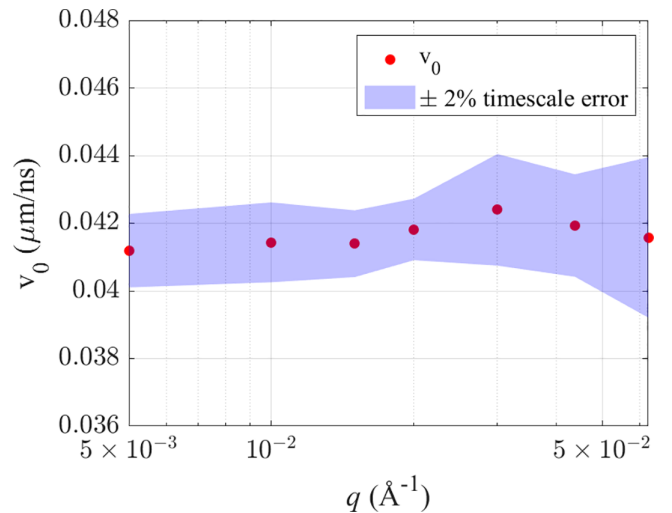

FIG. 28. The characteristic shear velocity, v_0, obtained from the simulated double-pulse XSVS using least-squares regression. The shaded errors are comparable to that of sequential-pulse XPCS [Fig. 12(a)] by having direct proportionality between contrast and $|F(q, \tau)|^2$.

where $G = Dq^2$ and $V = (v_0 q)^2$. This equation works well at small q, however, considerable numerical errors occur at large q is one caveat. The numerical errors are due to the product of an exponential approaching infinity as q increases and the difference of erf function with the limit of zero. Using the numerical integral in Eq. (36) is preferred as it behaves like the erf function with a positive asymptotic limit. The estimation of the diffusion coefficient in all these equations can be obtained through least-squares regression with the input arguments of the measured contrast function versus pulse time τ at different q values.

APPENDIX D: SUPPLEMENTARY FIGURES

Figure 20 shows the velocity spectrum of the turbulence field used in simulated XPCS. The spectrum follows Kolmogorov's $k^{-5/3}$ power law for 3D homogeneous isotropic turbulence and is the square of the *rms* velocity, $u_{\text{rms}}^{(k)}$, in Fig. 6.

Figure 21 shows the ratio of characteristic velocity to flow rms velocity for different mesh resolutions. The ratio variance is due to numerical errors of particle velocity interpolation while approaching the grid size. The decreasing ratio has limited impact on the multiscale theory even with an increasing spectrum (more kinetic energy at small scales) discussed in Sec. III B.

Figure 22 provides the velocity spectrum of the synthetically modified field used in simulated XPCS. With a power law of $k^{4/3}$ at large scales, the kinetic energy content is shifted to smaller scales. The theory of multiscale flow is validated using this flow field even though the peak of kinetic energy is close to k_{cutoff}. The scaling of the spectrum is the square of the rms velocity, $u_{\text{rms}}^{\prime(k)}$, in Fig. 9.

Figure 23 shows almost equivalent scaling between $v_0^{(k)}$ and $u_{\text{rms}}^{\prime(k)}$ for the synthetically modified multiscale flow. The average value of $c^{(k)}$ for $k \leqslant 16\,\mu\text{m}^{-1}$ is 0.482 still close to the ratio obtained for the synthetically modified multiscale flow $c^{\text{multiscale}} = 0.461$, while the discrepancy is larger compared to the original multiscale flow by having more energy weighted in the decreasing $c^{(k)}$ region.

Figure 24 is an estimation of D using the explicit formula in Eq. (32), which provides a fast way to examine D. However, it introduces poorer statistics with the timescale variance compared to the least-squares regression method in Fig. 11(a) since only two q values are considered.

Figures 25 and 26 are D and v_0 obtained from single-pulse XSVS, where more errors are introduced as compared to that of sequential-pulse XPCS [Figs. 11(a) and 12] and double-pulse XSVS (Figs. 27 and 28). The numerical errors are due to the integral over intensity distribution from discrete rather than continuous speckle patterns in time.

Figures 27 and 28 are D and v_0 obtained from double-pulse XSVS, where the errors are comparable to those of sequential-pulse XPCS [Figs. 11(a) and 12], since the contrast is determined by the same $|F(q, \tau)|^2$ in double-pulse XSVS.

[1] B. Berne and R. Pecora, *Dynamic Light Scattering: With Applications to Chemistry, Biology, and Physics* (Dover, New York, 2000).

[2] A. R. Sandy, Q. Zhang, and L. B. Lurio, Hard x-ray photon correlation spectroscopy methods for materials studies, Annu. Rev. Mater. Res. **48**, 167 (2018).

[3] T. Zemb and P. Lindner, Neutron, x-rays and light. Scattering methods applied to soft condensed matter, Mater. Today **5**, 38 (2002).

[4] R. P. Redouane Borsali, *Soft Matter Characterization* (Springer, Berlin, 2008), pp. 335–372.

[5] P. Emma, R. Akre, J. Arthur, R. Bionta, C. Bostedt, J. Bozek, A. Brachmann, P. Bucksbaum, R. Coffee, F. Decker, Y. Ding, D. Dowell, S. Edstrom, A. Fisher, J. Frisch, S. Gilevich, J. Hastings, G. Hays, P. Hering, Z. Huang *et al.*, First lasing and operation of an ångstrom-wavelength free-electron laser, Nature Photon. **4**, 641 (2010).

[6] T. Ishikawa, H. Aoyagi, T. Asaka, Y. Asano, N. Azumi, T. Bizen, H. Ego, K. Fukami, T. Fukui, Y. Furukawa, S. Goto, H. Hanaki, T. Hara, T. Hasegawa, T. Hatsui, A. Higashiya, T. Hirono, N. Hosoda, M. Ishii, T. Inagaki *et al.*, A compact x-ray free-electron laser emitting in the sub-ångström region, Nature Photon. **6**, 540 (2012).

[7] F.-J. Decker, K. L. Bane, W. Colocho, S. Gilevich, A. Marinelli, J. C. Sheppard, J. L. Turner, J. J. Turner, S. L. Vetter, A. Halavanau, C. Pellegrini, and A. A. Lutman, Tunable x-ray free electron laser multi-pulses with nanosecond separation, Sci. Rep. **12**, 3253 (2022).

[8] S. B. Dierker, R. Pindak, R. M. Fleming, I. K. Robinson, and L. Berman, X-ray photon correlation spectroscopy study of brownian motion of gold colloids in glycerol, Phys. Rev. Lett. **75**, 449 (1995).

[9] G. Grübel and F. Zontone, Correlation spectroscopy with coherent x-rays, J. Alloys Compd. **362**, 3 (2004), in Proceedings of the Sixth International School and Symposium on Synchrotron Radiation in Natural Science (ISSRNS).

[10] O. G. Shpyrko, X-ray photon correlation spectroscopy, J. Synchrotron. Radiat. **21**, 1057 (2014).

[11] E. Jakeman, *Photon Correlation and Light Beating Spectroscopy* (Springer, Berlin, 1974).

[12] H. Tennekes and J. L. Lumley, *Statistical Optics* (John Wiley & Sons, New York, 2015).

[13] P. Grabowski, S. Hansen, M. Murillo, L. Stanton, F. Graziani, A. Zylstra, S. Baalrud, P. Arnault, A. Baczewski, L. Benedict, C. Blancard, O. Čertík, J. Clérouin, L. Collins, S. Copeland, A. Correa, J. Dai, J. Daligault, M. Desjarlais, M. Dharma-Wardana *et al.*, Review of the first charged-particle transport coefficient comparison workshop, High Energy Density Phys. **37**, 100905 (2020).

[14] L. J. Stanek, A. Kononov, S. B. Hansen, B. M. Haines, S. X. Hu, P. F. Knapp, M. S. Murillo, L. G. Stanton, H. D. Whitley, S. D. Baalrud, L. J. Babati, A. D. Baczewski, M. Bethkenhagen, A. Blanchet, R. C. Clay, K. R. Cochrane, L. A. Collins, A. Dumi, G. Faussurier, M. French *et al.*, Review of the second charged-particle transport coefficient code comparison workshop, Phys. Plasmas **31**, 052104 (2024).

[15] N. Acharya, H. Pantell, D. Polsin, J. Rygg, G. Collins, P. Celliers, R. Betti, A. Gleason, H. Aluie, and J. Shang, Rippled shock propagation in a laser-driven target at multimegabar pressures, J. Appl. Phys. **137**, 115902 (2025).

[16] J. Carnis, W. Cha, J. Wingert, J. Kang, Z. Jiang, S. Song, M. Sikorski, A. Robert, C. Gutt, S.-W. Chen, Y. Dai, Y. Ma, H. Guo, L. B. Lurio, O. Shpyrko, S. Narayanan, M. Cui, I. Kosif, T. Emrick, T. P. Russell *et al.*, Demonstration of feasibility of x-ray free electron laser studies of dynamics of nanoparticles in entangled polymer melts, Sci. Rep. **4**, 6017 (2014).

[17] L. Shen, V. Esposito, N. G. Burdet, M. Zhu, A. N. Petsch, T. P. Croft, S. P. Collins, Z. Ren, F. Westermeier, M. Sprung, S. M. Hayden, J. J. Turner, and E. Blackburn, Interplay between relaxational atomic fluctuations and charge density waves in $La_{2-x}Sr_xCuO_4$, Phys. Rev. B **108**, L201111 (2023).

[18] Z. Porter, L. Shen, R. Plumley, N. G. Burdet, A. N. Petsch, J. Wen, N. C. Drucker, C. Peng, X. M. Chen, A. Fluerasu, E. Blackburn, G. Coslovich, D. G. Hawthorn, and J. J. Turner, Understanding the superconductivity and charge density wave interaction through quasi-static lattice fluctuations, Proc. Natl. Acad. Sci. USA **121**, e2412182121 (2024).

[19] M. Sutton, A review of x-ray intensity fluctuation spectroscopy, C. R. Phys. **9**, 657 (2008), Synchrotron x-rays and condensed matter.

[20] F. Lehmkühler, W. Roseker, and G. Grübel, From femtoseconds to hours—measuring dynamics over 18 orders of magnitude with coherent x-rays, Appl. Sci. **11**, 6179 (2021).

[21] K. Kurzer-Ogul, B. M. Haines, D. S. Montgomery, S. Pandolfi, J. P. Sauppe, A. F. Leong, D. Hodge, P. M. Kozlowski, S. Marchesini, E. Cunningham *et al.*, Radiation and heat transport in divergent shock–bubble interactions, Phys. Plasmas **31** (2024).

[22] A. F. Leong, D. S. Hodge, K. Kurzer-Ogul, S. Marchesini, S. Pandolfi, Y. Liu, J. L. Barber, K. Li, A. Sakdinawat, E. C. Galtier *et al.*, Combined speckle-and propagation-based single shot two-dimensional phase retrieval method, Opt. Express **32**, 46939 (2024).

[23] M. W. Guetg, A. A. Lutman, Y. Ding, T. J. Maxwell, F.-J. Decker, U. Bergmann, and Z. Huang, Generation of high-power high-intensity short x-ray free-electron-laser pulses, Phys. Rev. Lett. **120**, 014801 (2018).

[24] C. DeCaro, V. N. Karunaratne, S. Bera, L. B. Lurio, A. R. Sandy, S. Narayanan, M. Sutton, J. Winans, K. L. Duffin, J. Lehuta, and N. T. Karonis, X-ray speckle visibility spectroscopy in the single-photon limit, J. Synchrotron Radiat. **20**, 332 (2013).

[25] L. Li, P. Kwaśniewski, D. Orsi, L. Wiegart, L. Cristofolini, C. Caronna, and A. Fluerasu, Photon statistics and speckle visibility spectroscopy with partially coherent x-rays, J. Synchrotron Radiat. **21**, 1288 (2014).

[26] W. Jo, F. Westermeier, R. Rysov, O. Leupold, F. Schulz, S. Tober, V. Markmann, M. Sprung, A. Ricci, T. Laurus, A. Aschkan, A. Klyuev, U. Trunk, H. Graafsma, G. Grübel, and W. Roseker, Nanosecond x-ray photon correlation spectroscopy using pulse time structure of a storage-ring source, IUCrJ **8**, 124 (2021).

[27] F. Perakis, G. Camisasca, T. J. Lane, A. Späh, K. T. Wikfeldt, J. A. Sellberg, F. Lehmkühler, H. Pathak, K. H. Kim, K. Amann-Winkel, S. Schreck, S. Song, T. Sato, M. Sikorski, A. Eilert, T. McQueen, H. Ogasawara, D. Nordlund, W. Roseker, J. Koralek *et al.*, Coherent x-rays reveal the influence of cage effects on ultrafast water dynamics, Nature Commun. **9**, 1917 (2018).

[28] J. Möller, M. Reiser, J. Hallmann, U. Boesenberg, A. Zozulya, H. Rahmann, A.-L. Becker, F. Westermeier, T. Zinn, M. Sprung, T. Narayanan, C. Gutt, and A. Madsen, Using low dose x-ray speckle visibility spectroscopy to study dynamics of soft matter samples, New J. Phys. **23**, 093041 (2021).

[29] J. Verwohlt, M. Reiser, L. Randolph, A. Matic, L. A. Medina, A. Madsen, M. Sprung, A. Zozulya, and C. Gutt, Low dose x-ray speckle visibility spectroscopy reveals nanoscale dynamics in radiation sensitive ionic liquids, Phys. Rev. Lett. **120**, 168001 (2018).

[30] L. Shen, M. Seaberg, E. Blackburn, and J. J. Turner, A snapshot review—fluctuations in quantum materials: From skyrmions to superconductivity, MRS Adv. **6**, 221 (2021).

[31] B. A. Remington, H.-S. Park, D. T. Casey, R. M. Cavallo, D. S. Clark, C. M. Huntington, C. C. Kuranz, A. R. Miles, S. R. Nagel, K. S. Raman, and V. A. Smalyuk, Rayleigh-Taylor instabilities in high-energy density settings on the national ignition facility, Proc. Natl. Acad. Sci. USA **116**, 18233 (2018).

[32] N. Acharya, H. Aluie, and J. Shang, Numerical investigation of laser-driven shock interaction with a deformable particle, Phys. Plasmas **29**, 052302 (2022).

[33] S. C. Miller and V. N. Goncharov, Instability seeding mechanisms due to internal defects in inertial confinement fusion targets, Phys. Plasmas **29**, 082701 (2022).

[34] D. S. Hodge, A. F. Leong, S. Pandolfi, K. Kurzer-Ogul, D. S. Montgomery, H. Aluie, C. Bolme, T. Carver, E. Cunningham, C. B. Curry *et al.*, Multi-frame, ultrafast, x-ray microscope for imaging shockwave dynamics, Opt. Express **30**, 38405 (2022).

[35] S. Davidovits, C. Federrath, R. Teyssier, K. S. Raman, D. C. Collins, and S. R. Nagel, Turbulence generation by shock interaction with a highly nonuniform medium, Phys. Rev. E **105**, 065206 (2022).

[36] A. Fluerasu, A. Moussaïd, P. Falus, H. Gleyzolle, and A. Madsen, X-ray photon correlation spectroscopy under flow, J. Synchrotron Radiat. **15**, 378 (2008).

[37] S. Busch, T. H. Jensen, Y. Chushkin, and A. Fluerasu, Dynamics in shear flow studied by x-ray photon correlation spectroscopy, Eur. Phys. J. E **26**, 55 (2008).

[38] A. Fluerasu, P. Kwasniewski, C. Caronna, F. Destremaut, J.-B. Salmon, and A. Madsen, Dynamics and rheology under continuous shear flow studied by x-ray photon correlation spectroscopy, New J. Phys. **12**, 035023 (2010).

[39] W. R. Burghardt, M. Sikorski, A. R. Sandy, and S. Narayanan, X-ray photon correlation spectroscopy during homogenous shear flow, Phys. Rev. E **85**, 021402 (2012).

[40] X. Bian, J. K. Shang, E. G. Blackman, G. W. Collins, and H. Aluie, Scaling of turbulent viscosity and resistivity: Extracting a scale-dependent turbulent magnetic prandtl number, Astrophys. J. Lett. **917**, L3 (2021).

[41] D. M. Mills, *Third-Generation Hard X-Ray Synchrotron Radiation Sources: Source Properties, Optics, and Experimental Techniques* (Wiley & Sons, New York, 2002).

[42] F. Ehrburger-Dolle, I. Morfin, F. Bley, F. Livet, G. Heinrich, Y. Chushkin, and M. Sutton, Anisotropic and heterogeneous dynamics in stretched elastomer nanocomposites, Soft Matter **15**, 3796 (2019).

[43] H. Aluie, Compressible turbulence: The cascade and its locality, Phys. Rev. Lett. **106**, 174502 (2011).

[44] D. Radice, E. Abdikamalov, C. D. Ott, P. Mösta, S. M. Couch, and L. F. Roberts, Turbulence in core-collapse supernovae, J. Phys. G: Nucl. Part. Phys. **45**, 053003 (2018).

[45] C. Heaton, H. Yin, D. Khaghani, H. J. Lee, H. Poole, E. G. Blackman, N. Boiadjieva, C. Crépisson, G. W. Collins, A. Descamps, A. E. Gleason, C. Gutt, A. N. D. Petsch, L. Randolph, M. Nakatsutsumi, S. Nelson, P. McGehee, R. Plumley, C. Spindloe, T. Stevens *et al.*, Towards diffusivity measurements in laser shocked material with x-ray photon correlation spectroscopy, 2024, 66th Annual Meeting of the APS Division of Plasma Physics, https://meetings.aps.org/Meeting/DPP24/Session/NO09.3.

[46] H. Zhang, R. Betti, V. Gopalaswamy, R. Yan, and H. Aluie, Nonlinear excitation of the ablative Rayleigh-Taylor instability for all wave numbers, Phys. Rev. E **97**, 011203(R) (2018).

[47] D. Zhao, R. Betti, and H. Aluie, Scale interactions and anisotropy in Rayleigh–Taylor Turbulence, J. Fluid Mech. **930**, A29 (2022).

[48] D. Zhao and H. Aluie, Measuring scale-dependent shape anisotropy by coarse-graining: Application to inhomogeneous Rayleigh-Taylor turbulence, Phys. Rev. Fluids **8**, 114601 (2023).

[49] B. J. Ackerson and N. A. Clark, Dynamic light scattering at low rates of shear, J. Phys. France **42**, 929 (1981).

[50] T. Narayanan, C. Cheung, P. Tong, W. I. Goldburg, and X. lun Wu, Measurement of the velocity difference by photon correlation spectroscopy: An improved scheme, Appl. Opt. **36**, 7639 (1997).

[51] J.-P. Hansen and I. R. McDonald, *Theory of Simple Liquids with Applications to Soft Matter* (Academic Press, New York, 2013).

[52] C. Gutt, P. Wochner, B. Fischer, H. Conrad, M. Castro-Colin, S. Lee, F. Lehmkühler, I. Steinke, M. Sprung, W. Roseker, D. Zhu, H. Lemke, S. Bogle, P. H. Fuoss, G. B. Stephenson, M. Cammarata, D. M. Fritz, A. Robert, and G. Grübel, Single shot spatial and temporal coherence properties of the SLAC linac coherent light source in the hard x-ray regime, Phys. Rev. Lett. **108**, 024801 (2012).

[53] S. Mohanty, C. B. Cooper, H. Wang, M. Liang, and W. Cai, Computational approaches to model x-ray photon correlation spectroscopy from molecular dynamics, Modell. Simul. Mater. Sci. Eng. **30**, 075004 (2022).

[54] N. Wiener, *Time Series* (MIT Press, Cambridge, 1964).

[55] N. Jiang, M. K. Endoh, and T. Koga, 'Marker' grazing-incidence x-ray photon correlation spectroscopy: A new tool to peer into the interfaces of nanoconfined polymer thin films, Polymer J. **45**, 26 (2013).

[56] W. Roseker, S. O. Hruszkewycz, F. Lehmkühler, M. Walther, H. Schulte-Schrepping, S. Lee, T. Osaka, L. Strüder, R. Hartmann, M. Sikorski, S. Song, A. Robert, P. H. Fuoss, M. Sutton, G. B. Stephenson, and G. Grübel, Towards ultrafast dynamics with split-pulse x-ray photon correlation spectroscopy at free electron laser sources, Nature Commun. **9**, 1704 (2018).

[57] R. Mhanna, M. Giroux, K. J. T. Livi, C. Wang, A. Fluerasu, L. Wiegart, Y. Zhang, M. Sutton, and R. L. Leheny, Extremely slow diffusion of gold nanoparticles under confinement in mesoporous silica, J. Phys. Chem. C **126**, 3614 (2022).

[58] R. L. Leheny, M. C. Rogers, K. Chen, S. Narayanan, and J. L. Harden, Rheo-XPCS, Curr. Opin. Colloid Interface Sci. **20**, 261 (2015).

[59] G. G. Fuller, J. M. Rallison, R. L. Schmidt, and L. G. Leal, The measurement of velocity gradients in laminar flow by homodyne light-scattering spectroscopy, J. Fluid Mech. **100**, 555 (1980).

[60] X.-L. Wu, D. J. Pine, P. M. Chaikin, J. S. Huang, and D. A. Weitz, Diffusing-wave spectroscopy in a shear flow, J. Opt. Soc. Am. B **7**, 15 (1990).

[61] G. Eyink, E. Vishniac, C. Lalescu, H. Aluie, K. Kanov, K. Bürger, R. Burns, C. Meneveau, and A. Szalay, Flux-freezing breakdown in high-conductivity magnetohydrodynamic turbulence, Nature (London) **497**, 466 (2013).

[62] H. Yin, J. K. Shang, E. G. Blackman, G. W. Collins, and H. Aluie, Energy transfer and scale dynamics in 2D and 3D laser-driven jets, Phys. Plasmas **30**, 092309 (2023).

[63] H. Aluie, Scale decomposition in compressible turbulence, Physica D **247**, 54 (2013).

[64] J. Wang, Y. Yang, Y. Shi, Z. Xiao, X. T. He, and S. Chen, Cascade of kinetic energy in three-dimensional compressible turbulence, Phys. Rev. Lett. **110**, 214505 (2013).

[65] G. L. Eyink and T. D. Drivas, Cascades and dissipative anomalies in compressible fluid turbulence, Phys. Rev. X **8**, 011022 (2018).

[66] X. Bian and H. Aluie, Decoupled cascades of kinetic and magnetic energy in magnetohydrodynamic turbulence, Phys. Rev. Lett. **122**, 135101 (2019).

[67] S. B. Pope, *Turbulent Flows* (Cambridge University Press, New York, 2000).

[68] Y. Li, E. Perlman, M. Wan, Y. Yang, C. Meneveau, R. Burns, S. Chen, A. Szalay, and G. Eyink, A public turbulence database cluster and applications to study lagrangian evolution of velocity increments in turbulence, J. Turbul. **9**, N31 (2008).

[69] A. Madsen, R. L. Leheny, H. Guo, M. Sprung, and O. Czakkel, Beyond simple exponential correlation functions and equilibrium dynamics in x-ray photon correlation spectroscopy, New J. Phys. **12**, 055001 (2010).

[70] O. Bikondoa and D. Carbone, X-ray photon correlation spectroscopy with coherent nanobeams: A numerical study, Crystals **10**, 766 (2020).

[71] M. Bin, M. Reiser, M. Filianina, S. Berkowicz, S. Das, S. Timmermann, W. Roseker, R. Bauer, J. Öström, A. Karina, K. Amann-Winkel, M. Ladd-Parada, F. Westermeier, M. Sprung, J. Möller, F. Lehmkühler, C. Gutt, and F. Perakis, Coherent x-ray scattering reveals nanoscale fluctuations in hydrated proteins, J. Phys. Chem. B **127**, 4922 (2023).

[72] A. Majumdar, H. Li, P. Muhunthan, A. Späh, S. Song, Y. Sun, M. Chollet, D. Sokaras, D. Zhu, and M. Ihme, Direct observation of ultrafast cluster dynamics in supercritical carbon dioxide using x-ray photon correlation spectroscopy, Nature Commun. **15**, 10540 (2024).

[73] H. Aluie, S. Rai, H. Yin, A. Lees, D. Zhao, S. M. Griffies, A. Adcroft, and J. K. Shang, Effective drift velocity from turbulent transport by vorticity, Phys. Rev. Fluids **7**, 104601 (2022).

[74] H. Tennekes and J. L. Lumley, *A First Course in Turbulence* (MIT Press, Cambridge, 1972).

[75] A. Banerjee, W. N. Kraft, and M. J. Andrews, Detailed measurements of a statistically steady Rayleigh–Taylor mixing layer from small to high atwood numbers, J. Fluid Mech. **659**, 127 (2010).

[76] Y. Zhou, Rayleigh–Taylor and Richtmyer–Meshkov instability induced flow, turbulence, and mixing. II, Phys. Rep. **723-725**, 1 (2017), Rayleigh–Taylor and Richtmyer–Meshkov instability induced flow, turbulence, and mixing. II.

[77] S. M. Rahman and O. San, A relaxation filtering approach for two-dimensional Rayleigh–Taylor instability-induced flows, Fluids **4**, 78 (2019).

[78] J.-B. Gorce and E. Falcon, Statistical equilibrium of large scales in three-dimensional hydrodynamic turbulence, Phys. Rev. Lett. **129**, 054501 (2022).

[79] V. Smalyuk, O. Hurricane, J. Hansen, G. Langstaff, D. Martinez, H.-S. Park, K. Raman, B. Remington, H. Robey, O. Schilling, R. Wallace, Y. Elbaz, A. Shimony, D. Shvarts, C. Di Stefano, R. Drake, D. Marion, C. Krauland, and C. Kuranz, Measurements of turbulent mixing due to Kelvin–Helmholtz instability in high-energy-density plasmas, High Energy Density Phys. **9**, 47 (2013).

[80] K. A. Flippo, F. W. Doss, E. C. Merritt, B. G. DeVolder, C. A. Di Stefano, P. A. Bradley, D. Capelli, T. Cardenas, T. R. Desjardins, F. Fierro, C. M. Huntington, J. L. Kline, L. Kot, S. Kurien, E. N. Loomis, S. A. MacLaren, T. J. Murphy, S. R. Nagel, T. S. Perry, R. B. Randolph *et al.*, Late-time mixing and turbulent behavior in high-energy-density shear experiments at high Atwood numbers, Phys. Plasmas **25**, 056315 (2018).

[81] F. Lehmkühler, P. Kwaśniewski, W. Roseker, B. Fischer, M. A. Schroer, K. Tono, T. Katayama, M. Sprung, M. Sikorski, S. Song, J. Glownia, M. Chollet, S. Nelson, A. Robert, C. Gutt, M. Yabashi, T. Ishikawa, and G. Grübel, Sequential single shot x-ray photon correlation spectroscopy at the sacla free electron laser, Sci. Rep. **5**, 17193 (2015).

[82] Y. Shinohara, T. Osaka, I. Inoue, T. Iwashita, W. Dmowski, C. W. Ryu, Y. Sarathchandran, and T. Egami, Split-pulse x-ray photon correlation spectroscopy with seeded x-rays from x-ray laser to study atomic-level dynamics, Nature Commun. **11**, 6213 (2020).

[83] T. M. Squires and T. G. Mason, Fluid mechanics of microrheology, Annu. Rev. Fluid Mech. **42**, 413 (2010).

[84] F. Otto, X. Sun, F. Schulz, C. Sanchez-Cano, N. Feliu, F. Westermeier, and W. J. Parak, X-ray photon correlation spectroscopy towards measuring nanoparticle diameters in biological environments allowing for the in situ analysis of their bio-nano interface, Small **18**, 2201324 (2022).

[85] A. S. Tremsin, J. V. Vallerga, O. H. W. Siegmund, J. S. Woods, L. E. D. Long, J. T. Hastings, R. J. Koch, S. A. Morley, Y. de Chuang, and S. Roy, Photon-counting MCP/timepix detectors for soft x-ray imaging and spectroscopic applications, J. Synchrotron Radiat. **28**, 1069 (2021).

[86] R. Bandyopadhyay, A. S. Gittings, S. S. Suh, P. K. Dixon, and D. J. Durian, Speckle-visibility spectroscopy: A tool to study time-varying dynamics, Rev. Sci. Instrum. **76**, 093110 (2005).

[87] C. Gutt, L.-M. Stadler, A. Duri, T. Autenrieth, O. Leupold, Y. Chushkin, and G. Grübel, Measuring temporal speckle correlations at ultrafast x-ray sources, Opt. Express **17**, 55 (2009).

[88] M. H. Seaberg, B. Holladay, J. C. T. Lee, M. Sikorski, A. H. Reid, S. A. Montoya, G. L. Dakovski, J. D. Koralek, G. Coslovich, S. Moeller, W. F. Schlotter, R. Streubel, S. D. Kevan, P. Fischer, E. E. Fullerton, J. L. Turner, F.-J. Decker, S. K. Sinha, S. Roy, and J. J. Turner, Nanosecond x-ray photon correlation spectroscopy on magnetic skyrmions, Phys. Rev. Lett. **119**, 067403 (2017).

[89] Y. Sun, F. J. Decker, J. Turner, S. Song, A. Robert, and D. Zhu, Pulse intensity characterization of the LCLS nanosecond double-bunch mode of operation, J. Synchrotron. Radiat. **25**, 642 (2018).

[90] W. Jo, S. Stern, F. Westermeier, R. Rysov, M. Riepp, J. Schmehr, J. Lange, J. Becker, M. Sprung, T. Laurus, H. Graafsma, I. Lokteva, G. Grübel, and W. Roseker, Single and multi-pulse based x-ray photon correlation spectroscopy, Opt. Express **31**, 3315 (2023).

[91] P. Falus, L. B. Lurio, and S. G. J. Mochrie, Optimizing the signal-to-noise ratio for x-ray photon correlation spectroscopy, J. Synchrotron Radiat. **13**, 253 (2006).

[92] J. Möller, M. Reiser, J. Hallmann, U. Boesenberg, A. Zozulya, H. Rahmann, A. L. Becker, F. Westermeier, T. Zinn, F. Zontone, C. Gutt, and A. Madsen, Implications of disturbed photon-counting statistics of eiger detectors for x-ray speckle visibility experiments, J. Synchrotron. Radiat. **26**, 1705 (2019).